The Next Generation Fornax Survey (NGFS). IV. Mass and Age Bimodality of Nuclear Clusters in the Fornax Core Region

Yasna Ordenes-Briceño, Thomas Puzia, Paul Eigenthaler, Matthew Taylor, Roberto Muñoz, Hongxin Zhang, Karla Alamo-Martínez, Karen Ribbeck, Eva Grebel, Simón Ángel, et al.

The Astrophysical Journal, 860:4 (20pp), 2018 June 10 https://doi.org/10.3847/1538-4357/aac1b8

The Next Generation Fornax Survey (NGFS). IV. Mass and Age Bimodality of Nuclear Clusters in the Fornax Core Region

Yasna Ordenes-Briceño[1,2,11], Thomas H. Puzia[1], Paul Eigenthaler[1,12], Matthew A. Taylor[3,13], Roberto P. Muñoz[1], Hongxin Zhang[4], Karla Alamo-Martínez[1,14], Karen X. Ribbeck[1], Eva K. Grebel[2], Simón Ángel[1], Patrick Côté[5], Laura Ferrarese[5], Michael Hilker[6], Ariane Lançon[7], Steffen Mieske[8], Bryan W. Miller[9], Yu Rong[1,12], and Ruben Sánchez-Janssen[10]

[1] Institute of Astrophysics, Pontificia Universidad Católica de Chile, Av. Vicuña Mackenna 4860, 7820436 Macul, Santiago, Chile; yordenes@astro.puc.cl
[2] Astronomisches Rechen-Institut, Zentrum für Astronomie der Universität Heidelberg, Mönchhofstraße 12-14, D-69120 Heidelberg, Germany
[3] Gemini Observatory, Northern Operations Center, 670 North A'ohoku Place, Hilo, HI 96720, USA
[4] CAS Key Laboratory for Research in Galaxies and Cosmology, Department of Astronomy, University of Science and Technology of China, Hefei 230026, People's Republic of China
[5] NRC Herzberg Astronomy and Astrophysics, 5071 West Saanich Road, Victoria, BC V9E 2E7, Canada
[6] European Southern Observatory, Karl-Schwarzchild-Str. 2, D-85748 Garching, Germany
[7] Observatoire Astronomique de Strasbourg, Université de Strasbourg, CNRS, UMR 7550, 11 rue de l'Universite, F-67000 Strasbourg, France
[8] European Southern Observatory, 3107 Alonso de Córdova, Vitacura, Santiago, Chile
[9] Gemini Observatory, South Operations Center, Casilla 603, La Serena, Chile
[10] STFC UK Astronomy Technology Centre, Royal Observatory, Blackford Hill, Edinburgh, EH9 3HJ, UK
Received 2018 February 13; revised 2018 April 17; accepted 2018 April 29; published 2018 June 6

Abstract

We present the analysis of 61 nucleated dwarf galaxies in the central regions ($\lesssim R_{\rm vir}/4$) of the Fornax galaxy cluster. The galaxies and their nuclei are studied as part of the Next Generation Fornax Survey using optical imaging obtained with the Dark Energy Camera mounted at Blanco/Cerro Tololo Inter-American Observatory and near-infrared data obtained with VIRCam at VISTA/ESO. We decompose the nucleated dwarfs in nucleus and spheroid, after subtracting the surface brightness profile of the spheroid component and studying the nucleus using point source photometry. In general, nuclei are consistent with colors of confirmed metal-poor globular clusters, but with significantly smaller dispersion than other confirmed compact stellar systems in Fornax. We find a bimodal nucleus mass distribution with peaks located at $\log(\mathcal{M}_*/M_\odot) \simeq 5.4$ and ∼6.3. These two nucleus subpopulations have different stellar population properties: the more massive nuclei are older than ∼2 Gyr and have metal-poor stellar populations ($Z \leqslant 0.02\,Z_\odot$), while the less massive nuclei are younger than ∼2 Gyr with metallicities in the range $0.02 < Z/Z_\odot \leqslant 1$. We find that the nucleus mass ($\mathcal{M}_{\rm nuc}$) versus galaxy mass ($\mathcal{M}_{\rm gal}$) relation becomes shallower for less massive galaxies starting around $10^8\,M_\odot$, and the mass ratio $\eta_n = \mathcal{M}_{\rm nuc}/\mathcal{M}_{\rm gal}$ shows a clear anticorrelation with $\mathcal{M}_{\rm gal}$ for the lowest masses, reaching 10%. We test current theoretical models of nuclear cluster formation and find that they cannot fully reproduce the observed trends. A likely mixture of in situ star formation and star cluster mergers seems to be acting during nucleus growth over cosmic time.

Key words: galaxies: clusters: individual (Fornax) – galaxies: dwarf – galaxies: nuclei

1. Introduction

Dwarf galaxies dominate the galaxy number density in dense environments. Whether they contain a compact stellar nucleus at their centers or not is an important distinction among the dwarf galaxy population. Nuclear clusters are very dense stellar systems with sizes similar to globular cluster (GCs, ∼3–10 pc; Böker et al. 2004; Côté et al. 2006; Turner et al. 2012; den Brok et al. 2014; Georgiev & Böker 2014; Puzia et al. 2014) but with a broader range of masses 10^5 to $10^8\,M_\odot$ (e.g., Walcher et al. 2006; Georgiev et al. 2016; Spengler et al. 2017). Nuclei are a common characteristic in galaxies, from dwarfs to giants. The nucleation fraction can reach around 70%–80% and is independent of the galaxy morphology (Böker et al. 2004; Côté et al. 2006; Georgiev et al. 2009; Turner et al. 2012; den Brok et al. 2014; Georgiev & Böker 2014; Muñoz et al. 2015; Eigenthaler et al. 2018). However, the nucleation fraction decreases with luminosity (e.g., Muñoz et al. 2015), going from as high as ∼90% for galaxies brighter than $M_i \leqslant -16$ mag to 0% for $M_i \leqslant -10$ mag. This may be related to instrument sensitivity limits, beyond which it becomes harder to detect the lowest surface brightness spheroids and, thus, to associate a nucleus with a low-surface-brightness galaxy spheroid. Toward the bright galaxy regime, it has been noticed that nuclei are no longer detected for galaxies with $M_B < -19.5$ mag. This might be related to the fact that the central parsecs of bright galaxies can have complex surface brightness profiles, which makes it difficult to separate the galaxy light from the nucleus light, if at all present (e.g., Côté et al. 2006; Turner et al. 2012). Another reason is that central supermassive black holes (SMBHs) coexisting with nuclear clusters can dissolve the central cluster if the SMBH is massive enough, increasing its sphere of influence to radii similar to those of the nuclear cluster (e.g., Antonini 2013).

Nuclear cluster studies have revealed several correlations between nuclei and their host galaxy, such as the nucleus-to-galaxy mass relation, their velocity dispersion and galaxy mass,[15] and the size–luminosity relation (Böker et al. 2004; Turner et al. 2012; Georgiev & Böker 2014; den Brok

[11] PUC-HD Graduate Student Exchange Fellow.
[12] CASSACA Postdoctoral Fellow.
[13] Gemini Science Fellow.
[14] FONDECYT Postdoctoral Fellow.
[15] For late-type galaxies, this would be the bulge mass.

et al. 2014; Spengler et al. 2017). These correlations indicate a connection between the nucleus and the formation of its parent galaxy. Furthermore, the stellar population properties of nuclei seem to be more complex than first thought, revealing multiple stellar populations rather than being old and metal-poor objects. Using spectra, Rossa et al. (2006) found in a sample of 40 late-type galaxies (LTGs) that the luminosity-weighted ages of half of the nuclei are younger than 1 Gyr, within a range from 10 Myr to very old ages $\gtrsim$10 Gyr (see also Walcher et al. 2006). For 26 early-type galaxies (ETGs) in the Virgo cluster, Paudel et al. (2011) found spectroscopic evidence that the age distribution of nuclei is dominated by young ages. In terms of metallicity, their work revealed a broad metallicity distribution of the nuclei, from -1.22 dex to $+0.18$ dex, which was wider than the host galaxy metallicity range. When analyzing age and metallicity distributions in radial profiles using bins along the major axis of the dwarf galaxies, Paudel et al. (2011) found that the inner bins are dominated by younger ages and broader metallicity distributions than outer regions. Spengler et al. (2017) observed in Virgo cluster galaxies that, on average, the nuclei and host galaxies have similar metallicities with a mean metallicity of 0.07 ± 0.3 dex, but if they exclude the galaxies that deviate from the mass–metallicity relation, then nuclei are on average 0.20 dex more metal-rich than their host galaxies. Clearly, conducting deep, homogeneous, panchromatic nuclear cluster searches, based on wide-field imaging data, will allow us to focus on the faint *and* bright nucleated galaxy regime at the same time and may help put some of these seemingly contradictory observations in context.

Considerable observational efforts were recently undertaken to map the nearby galaxy cluster regions in Virgo and Fornax, with deep, homogeneous wide-field surveys reaching low-surface-brightness dwarf galaxies ($\langle\mu_{e,i}\rangle \simeq 29$ mag arcsec^{-2}; see, e.g., Mihos et al. 2005, 2017; Ferrarese et al. 2012; Muñoz et al. 2015; Eigenthaler et al. 2018). This is the case for the *Next Generation Fornax Survey* (NGFS), which covers a large area of the Fornax galaxy cluster with optical and near-infrared observations. The NGFS team has identified 258 dwarf galaxy candidates in the central Fornax regions ($R_{\rm NGC1399} \leqslant 350$ kpc). From the total sample (258), only 75 dwarfs are nucleated (29%; Eigenthaler et al. 2018). So far, the faintest nucleated dwarf candidate in the NGFS sample has an absolute magnitude of $M_i \simeq -10.8$ mag, indicating that the luminosity ratio between the nucleus and the host spheroid $\eta_L = \mathcal{L}_{\rm nucleus}/\mathcal{L}_{\rm spheroid}$ is significantly higher for the faint galaxies than previously thought. Earlier studies of bright ETGs found $\langle\eta_L\rangle = 0.41\%$ in Fornax (Turner et al. 2012) and $\langle\eta_L\rangle = 0.3\%$ for Virgo (Côté et al. 2006). The NGFS sample pushes the study of galaxy nuclei into the faint luminosity regime. In dense galaxy cluster environments, nucleated galaxies have been studied up to now in galaxies brighter than $M_i \simeq -15$ mag in Fornax and Virgo (Côté et al. 2006; Turner et al. 2012) using the Advance Camera Survey (ACS) in the *Hubble Space Telescope* (*HST*), with a sample of 31 and 45 nuclei, respectively.

In this work, we explore, for the first time, the faint nucleated dwarf galaxy luminosity regime in terms of its photometric properties and scaling relations. We assume a distance modulus of 31.51 ± 0.03 mag for Fornax, which corresponds to a distance of 20 Mpc (Blakeslee et al. 2009). The derived magnitudes in optical passbands are all in the AB system, and the near-infrared magnitudes were transformed from Vega to the AB system using $\Delta m_{K_s} = 1.85$ mag and $\Delta m_J = 0.91$ mag (Blanton & Roweis 2007).

2. Observations

The Next Generation Fornax Survey is an ongoing, deep multiwavelength survey that covers the entire Fornax galaxy cluster out to its virial radius (1.5 Mpc). NGFS uses the Cerro Tololo Inter-American Observatory (CTIO) 4 m Blanco telescope in combination with the Dark Energy Camera (DECam; Flaugher et al. 2015) for optical photometry, as well as the European Southern Observatory (ESO) 3.7 m VISTA telescope and VIRCam (Sutherland et al. 2015) for near-infrared (NIR) photometry. The current NGFS survey footprint covers 50 deg^2 with 19 DECam tiles of 2.65 deg^2 each and detects point sources at signal-t0-noise ratio (S/N) = 5 down to $u' = 26.5$, $g' = 26.1$, $i' = 25.3$, $J = 24.0$, and $K_s = 23.3$ AB mag, which corresponds to the GC luminosity function (GCLF) turnover at $M_V \simeq -7.4$ mag (e.g., Rejkuba 2012).

Details on the reduction process and photometry will be provided in a forthcoming paper (T. H. Puzia et al. 2018, in preparation). In the following, we give a brief summary of the main survey characteristics. The DECam data have been processed using the basic calibrated images delivered by the DECam Community pipeline (v2.5.0 Valdes et al. 2014), which were corrected for bias, flat fielding, and image crosstalk. In subsequent steps, we applied our custom background-subtraction strategy. The astrometry, photometric calibration, and stacking were performed with the software SCAMP (v2.2.6; Bertin 2006), Source Extractor (SE, v2.19.5; Bertin & Arnouts 1996), and SWARP (v2.19.5; Bertin et al. 2002). The reference stars are from the 2MASS Point Source Catalog (Skrutskie et al. 2006) and the SDSS stripe 82 standard star frames (Abazajian et al. 2009). Our optical-passband photometry was also cross-validated using previous catalogs of the same sky area, specifically with the data provided in the work of Kim et al. (2013), who obtained photometry in the U, B, V, and I passbands, taken with the Mosaic II camera at the 4 m Blanco telescope at CTIO. The average seeing on the stacked images is $2\farcs06 \pm 0\farcs09$, $1\farcs38 \pm 0\farcs06$, and $1\farcs23 \pm 0\farcs02$ in the u', g', and i' filters, respectively. The pixel scale of our final DECam image stacks is $0\farcs263$, which corresponds to 25.5 pc at the distance of the Fornax cluster.

The NIR VIRCam observations were processed from scratch starting with the raw data, for which we developed a custom pipeline to do the basic calibration as well as the background modeling and subtraction, photometry, astrometric calibration, and the final image stacking. This was done with the same software packages as described for the optical DECam data reduction. The average seeing on the stacked J and K_s images is $0\farcs87 \pm 0\farcs03$ and $0\farcs89 \pm 0\farcs05$, respectively. The spatial resolution of the VISTA data is $0\farcs34/\mathrm{pix} = 33$ pc at the distance of Fornax. The survey information and data reduction process of the near-infrared and optical observations will be presented in a forthcoming paper (T. H. Puzia et al. 2018, in preparation).

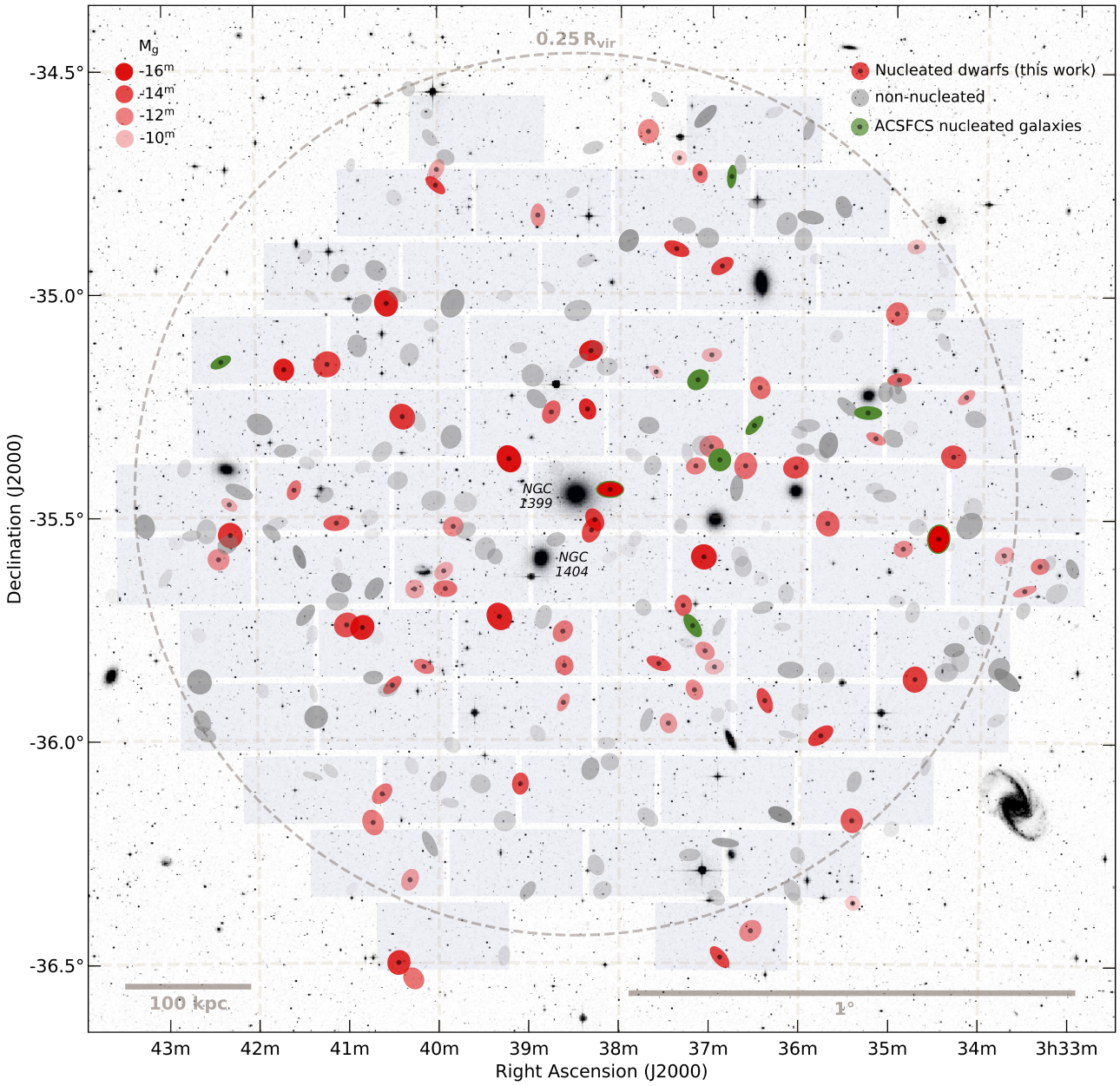

Figure 1. Central region of the Fornax galaxy cluster of the inner ∼25% of the virial radius ($R_{vir}/4$, see dashed circle), showing the spatial distribution of nucleated dwarfs (red symbols), nonnucleated dwarfs (gray symbols), and the nucleated galaxies studied by the ACSFCS (green symbols; see Côté et al. 2006). The field is centered on the giant elliptical cD galaxy NGC 1399, which is located at the center of the field. The symbol transparency parameterizes the galaxy luminosity as indicated in the top left corner: more-transparent symbols indicate fainter galaxies, while the ellipticity and position angle of the symbol represent the same parameters of the corresponding galaxy spheroid. Two red ellipses with green edges mark the two dwarf galaxies (FCC 202 and FCC 136) that are included in both the ACSFCS sample and this work.

3. Analysis

3.1. Sample Selection

The nucleated dwarf galaxy sample of this work originates in the NGFS sample studied by Eigenthaler et al. (2018), which consists of 258 dwarf galaxies in the inner 25% of the virial radius of the Fornax cluster ($R_{vir}/4 \simeq 350$ kpc; Drinkwater et al. 2001) centered on the cD galaxy NGC 1399 (see Figure 1). Of this total dwarf galaxy population, we consider 75 (29%) to be nucleated based on the following selection criteria: (1) the central object is located at the photometric center of the spheroid or slightly offset ($\leqslant 3''$), (2) the nuclear cluster is detected in at least two filters, and (3) the central object appears as a point source. From the 75 nucleated dwarfs, we could further analyze 61 nuclei. For six galaxies, the surface brightness profile fits of their spheroid light did not converge to robust solutions, due to contamination by nearby objects or too-low surface brightness values. For eight of them that have good spheroid profile fits, we encountered unstable solutions in the very inner regions, mainly due to saturation of nearby sources, too-low S/N, or stacking artifacts in the area. Since we are primarily interested in robust panchromatic photometry, we, therefore, exclude these objects from the subsequent analysis. Two nucleated dwarf galaxies in our

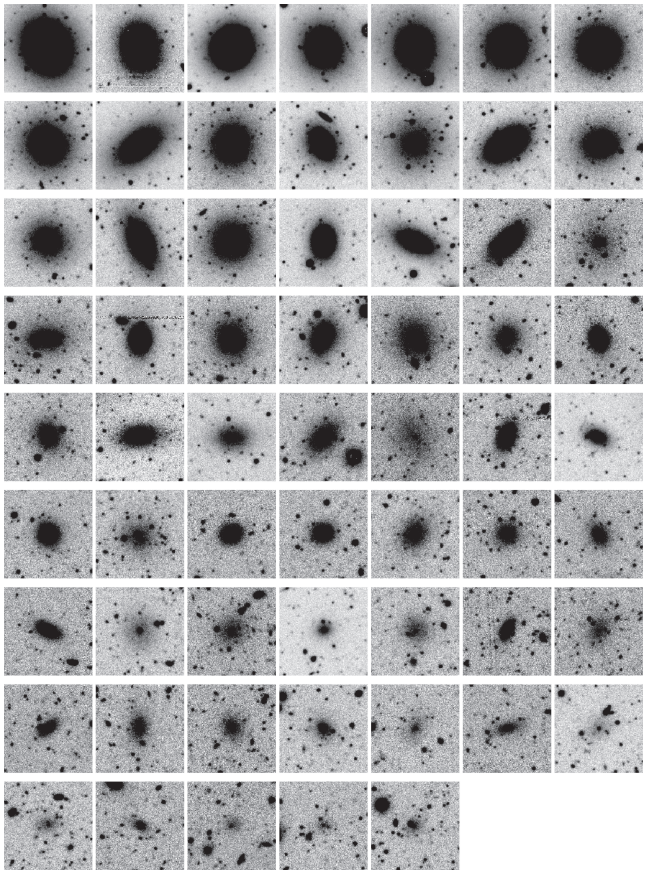

Figure 2. Postage stamp g'-band images for the 61 nucleated dwarfs, sorted by the g'-band luminosity of their spheroid component, which is well approximated by a Sérsic profile (see Eigenthaler et al. 2018). Each image has 200×200 pix^2, corresponding to 5.1×5.1 kpc^2 at the Fornax distance.

sample overlap with the ACS Fornax Cluster Survey sample (Côté et al. 2006), FCC202 and FCC136, which are shown in Figure 1 as red ellipses with green edges.

Even with subarcsecond seeing, the spatial resolution of DECam (1 pix = 25.5 pc) and VISTA (1 pix = 33 pc), all nuclei at the Fornax distance are unresolved point sources. Nucleus detections in the central NGFS data set for each filter reach these magnitudes: $u' \simeq 25.2$ mag, $g' \simeq 26.2$ mag, $i' \simeq 25$ mag, $J \simeq 21.9$ mag, and $K_s \simeq 23.1$ mag. The faintest nucleated dwarf galaxy detected in the Fornax central region has an absolute magnitude of $M_i \simeq -10.8$ mag.

Figure 2 shows the gallery of g'-band images of our nucleated dwarf galaxy sample, ordered by decreasing luminosity of their spheroid component from top left to bottom right. It is worth noting that the spheroid axis ratios and position angles of the dwarf galaxies are mostly consistent with rounded systems ($\epsilon < 0.55$; see Eigenthaler et al. 2018). Although the ellipticity distributions of the spheroid light components[16] of nucleated and nonnucleated dwarfs cover a similar range, Eigenthaler et al. showed that the nucleated dwarfs are systematically rounder than their nucleus-devoid counterparts by $\Delta\epsilon \approx 0.1$. In addition, the spheroids of nucleated dwarfs have on average larger half-light radii ($\Delta r_{\rm eff} \approx 0.2$–$0.3$ kpc) than nonnucleated dwarfs.

[16] This considers only the spheroid light component of the dwarf galaxy, excluding the nuclear star cluster.

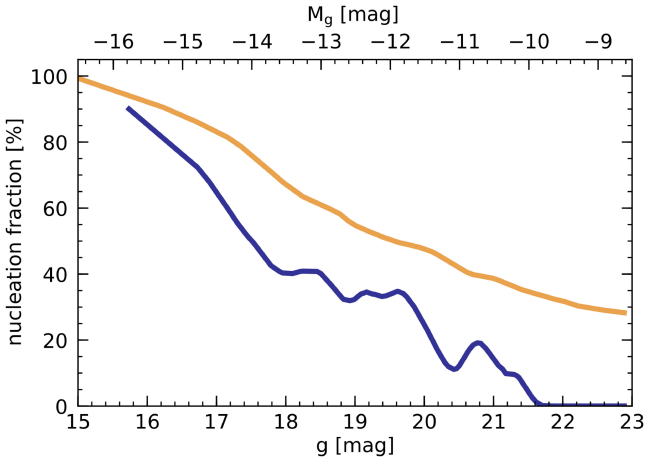

Figure 3. Nucleation fraction ($f_{\rm nuc}$) of Fornax dwarfs as a function of g'-band galaxy luminosity. The orange line shows the cumulative distribution ($f_{\rm nuc}[<g']$), while the blue curve illustrates the differential relation ($\Delta f_{\rm nuc}/\Delta g'$).

We also observe that toward lower galaxy luminosities, the nucleus luminosity becomes more prominent than the luminosity of the galaxy spheroid, something that contrasts with the relation found for bright galaxies (Turner et al. 2012). Our main goal in this article is, therefore, to characterize the faint population of nuclear star clusters in the dwarf galaxies in the central Fornax region in terms of the information provided by their luminosities and colors using the broad spectral energy distribution (SED) coverage of our NGFS filter set.

3.2. Spatial Distribution

Figure 1 shows how our nucleated dwarf sample improves the sample size in terms of spatial coverage and luminosity range compared to previous studies in the same region, in particular those based on the ACSFCS observations, which included nine nucleated dwarf galaxies. The spatial distribution of the nucleated dwarfs in the central Fornax region follows the spatial distribution of the nonnucleated dwarf galaxy population, with a slight anisotropy in the east–west direction, where the dwarf galaxy surface density appears to be mildly elevated compared to the north–south direction and with individual density peaks that follow the distribution of the giant galaxies (see Muñoz et al. 2015). Our earlier studies indicated that there may be a higher clustering of dwarf galaxies on length scales below ∼100 kpc. In galactocentric distance from NGC 1399, the nonnucleated sample shows a flat distribution out to ∼350 kpc; meanwhile the nucleated dwarfs have a peak in surface number density at a cluster-centric radius of ∼200 kpc and declining outward. Thus, data from the full NGFS survey footprint is required to understand the overall nucleated versus nonnucleated galaxy distribution in the Fornax galaxy cluster. Some intriguing results on this topic from the sample presented in this work will be addressed in the Discussion.

3.3. Nucleation Fraction

The nucleation fraction ($f_{\rm nuc}$) according to the previous work of Turner et al. (2012) for the Fornax region is 72%, with galaxy luminosities of their sample reaching as low as $M_B \simeq -16$ mag, thus only covering the bright galaxy regime. The NGFS nucleated dwarf galaxy sample extends this limit to $M_{g'} \simeq -10.5$ mag. In Muñoz et al. (2015), we have found that

$f_{\rm nuc}$ depends strongly on the galaxy luminosity. In Figure 3 we use the NGFS dwarf galaxy sample to estimate cumulative and differential $f_{\rm nuc}$ as a function of galaxy luminosity in a window of 20 galaxies and smooth it using a locally weighted scatter plot smoothing (LOWESS) fit (e.g., Cleveland 1981) to inspect the general trend. The blue and orange lines show the differential and cumulative $f_{\rm nuc}$ distributions, $\Delta f_{\rm nuc}/\Delta g'$ and $f_{\rm nuc}(<g')$, respectively. For the bright NGFS dwarf galaxies ($M_{g'} \lesssim -16$ mag), $f_{\rm nuc}$ reaches $\gtrsim$90%. On the other hand, fainter galaxies show systematically lower $f_{\rm nuc}$ values, reaching zero at absolute magnitudes $M_{g'} \simeq -10$ mag. Although finding nucleated dwarfs toward fainter magnitudes depends on both the point-source detection limit (see values in Section 3.1) and the surface brightness limit of our NGFS data ($\langle\mu_{i'}\rangle_e \approx 28$mag arcsec^{-2}; see Muñoz et al. 2015; Eigenthaler et al. 2018), it is unclear whether ultra-low-surface-brightness spheroids are nucleated or not, as there may be detected nuclei in our NGFS point-source catalogs for which our photometry failed to detect the surrounding ultra-low-surface-brightness spheroid. However, given the relatively faint point-source detection limit, we have a strong indication that for the sample of detected low-surface-brightness dwarf galaxy spheroids in Fornax, the nucleation stops at a well-defined galaxy luminosity ($M_{g'} \simeq -10$ mag), corresponding to a galaxy stellar mass of $\log \mathcal{M}_\star \approx 6.4$ (Eigenthaler et al. 2018).

3.4. Morphological Decomposition of Nucleus and Spheroid

Nuclei studies are affected by the host galaxy luminosity, and, therefore, it is necessary to subtract the galaxy spheroid light in order to study their intrinsic properties. To accomplish this, we have developed an iterative approach to surface brightness profile fitting of dwarf galaxies using GALFIT (v3.0.5; Peng et al. 2002) and Sérsic models in the $u'g'i'$ bands (for more details, see Eigenthaler et al. 2018) and in the JK_s bands. The process to fit the light of a nucleated dwarf requires more iterations to achieve the best residual image, where the nucleus and spheroid are clearly separated. The procedure to fit dwarf galaxies is as follows. (1) A cutout image centered in the dwarf galaxy is created with size of $105'' \times 105''$ (10.2 kpc $\times$ 10.2 kpc). (2) A mask image is created to cover all of the sources around the dwarf, thus creating a "dwarf-only" image. (3) GALFIT is run over the cutout image using a point-spread function (PSF) model (created with PSFEX) and the mask. If the nucleus is present, a compact stellar object is left at or near the dwarf galaxy center. (4) The residual image is used to construct a new mask with the nucleus included. (5) The steps from (2) to (4) are repeated at least three times to obtain the best nucleus–spheroid decomposition, leaving a residual image including the nucleus only. Examples of the galaxy fitting process for two dwarf galaxies with different spheroid surface-brightness levels and ellipticities are shown in Figure 4. The dwarf galaxy images in the $u'g'i'$ filters are shown in the top row of panels, while the panels in the bottom row show the corresponding residual images after the subtraction of the spheroid component. The nucleus of each dwarf is clearly visible in the center of each residual image. In several cases, other compact objects are found near the nucleus, which could be potential satellite globular clusters. The analysis of the nucleus neighborhood and its constituent stellar populations will be presented in a forthcoming paper (Y. Ordenes-Briceño et al. 2018, in preparation).

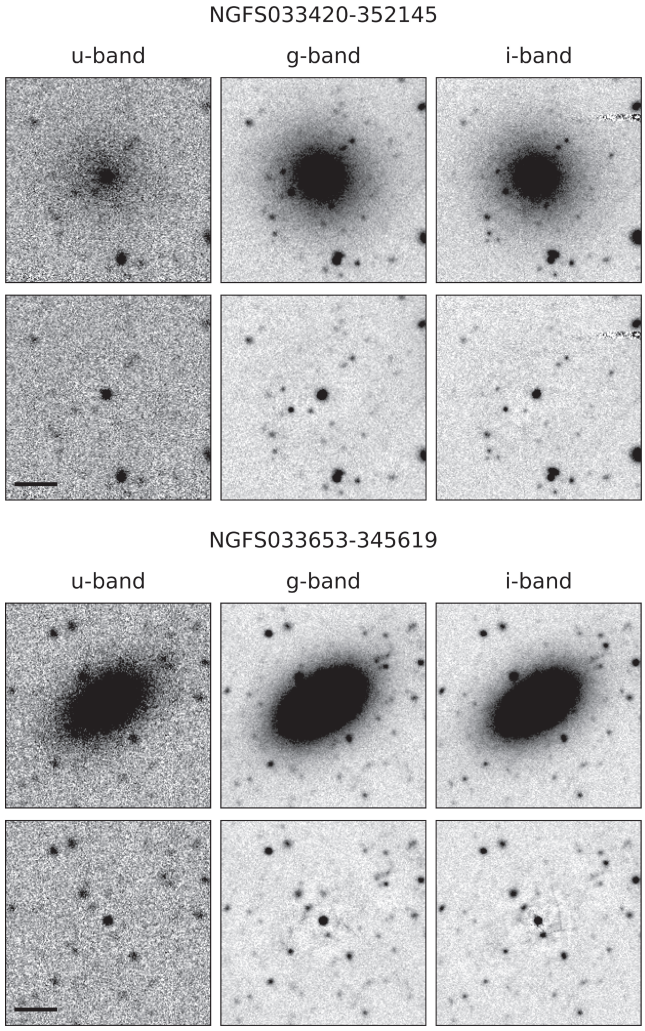

Figure 4. Illustration of the galaxy fitting for two dwarf galaxies in the three optical bands, $u'g'i'$ from left to right, respectively. The top row shows the original image, and the bottom row shows the best residual images (GALAXY—MODEL), where the nuclear star cluster is deliberately left in the center and is visible in all filters. A scale bar (solid line) is shown at the bottom left image corresponding to $10\farcs3 \triangleq 1$ kpc.

3.5. Photometry

After the spheroid-nucleus fitting procedure, we run SE with the corresponding PSF model and generate a catalog with the PSF photometry in all filters for each nucleus. From the 61 dwarf galaxies (see Figure 2), 60 nuclei remain with reliable i'-band, 59 with g'-band, 28 with u'- and K_s-band, and 43 with good J-band photometry. The reasons for this inhomogeneity are partially or nonoverlapping DECam and VISTA fields of view, bad S/N, or stacking in that area due to small overlap of the individual images or saturated or simply too faint nuclei. Photometry in $u'g'i'JK_s$ is available for 28 nuclei. Table 1 shows the coordinates, photometry, and stellar masses for the 61 nuclei. The photometry is corrected for foreground Galactic extinction with values taken from the latest Schlafly & Finkbeiner (2011) recalibration of the Schlegel et al. (1998) dust reddening maps. Reddening values for the different filters are calculated assuming the Fitzpatrick (1999) reddening law with $R_V = 3.1$. The average foreground extinction toward the central region of Fornax is measured according to the brightest

Table 1
Nuclear Star Cluster Parameters

Nucleus	R.A. (J2000) hh:mm:ss.ss	Decl.(J2000) dd:mm:ss.s	u' (AB mag)	g' (AB mag)	i' (AB mag)	J (AB mag)	K_s (AB mag)	$\log(\mathcal{M}_{*,\mathrm{nucleus}})$ ($M_\odot$)
NGFS033322-353620n	03:33:22.19	−35:36:20.2	⋯	24.078 ± 0.023	23.368 ± 0.023	⋯	⋯	$5.370^{+0.009}_{-0.008}$
NGFS033332-353942n	03:33:32.16	−35:39:42.3	⋯	24.543 ± 0.033	24.072 ± 0.044	⋯	⋯	$5.184^{+0.013}_{-0.013}$
NGFS033346-353455n	03:33:46.05	−35:34:56.0	⋯	25.335 ± 0.084	⋯	⋯	⋯	⋯
NGFS033412-351343n	03:34:12.18	−35:13:42.6	⋯	25.046 ± 0.052	23.735 ± 0.036	23.222 ± 0.101	⋯	$5.490^{+0.137}_{-0.041}$
NGFS033420-352145n	03:34:20.17	−35:21:44.7	⋯	21.712 ± 0.004	21.050 ± 0.004	20.740 ± 0.010	⋯	$6.310^{+0.227}_{-0.249}$
NGFS033444-355141n	03:34:44.17	−35:51:41.4	23.173 ± 0.034	22.169 ± 0.008	21.490 ± 0.006	21.289 ± 0.014	21.895 ± 0.053	$6.087^{+0.284}_{-0.269}$
NGFS033446-345334n	03:34:46.13	−34:53:34.2	⋯	25.351 ± 0.087	24.025 ± 0.062	⋯	⋯	$5.395^{+0.059}_{-0.066}$
NGFS033453-353411n	03:34:52.74	−35:34:10.7	⋯	25.883 ± 0.116	24.942 ± 0.096	⋯	⋯	$4.804^{+0.106}_{-0.087}$
NGFS033456-351127n	03:34:56.49	−35:11:27.0	24.360 ± 0.085	23.195 ± 0.015	22.494 ± 0.014	22.415 ± 0.041	22.520 ± 0.096	$5.658^{+0.215}_{-0.261}$
NGFS033458-350235n	03:34:58.21	−35:02:33.9	⋯	22.424 ± 0.007	21.736 ± 0.007	21.533 ± 0.024	⋯	$6.010^{+0.240}_{-0.253}$
NGFS033512-351923n	03:35:11.50	−35:19:22.6	25.020 ± 0.162	23.638 ± 0.018	22.997 ± 0.018	22.775 ± 0.052	22.724 ± 0.101	$5.460^{+0.354}_{-0.267}$
NGFS033524-362150n	03:35:24.08	−36:21:50.7	⋯	⋯	19.645 ± 0.004	19.555 ± 0.008	19.632 ± 0.013	$6.562^{+0.118}_{-0.230}$
NGFS033525-361044n	03:35:25.20	−36:10:44.2	24.796 ± 0.113	23.662 ± 0.020	22.911 ± 0.019	22.390 ± 0.049	18.202 ± 0.003	$5.655^{+0.229}_{-0.281}$
NGFS033543-353051n	03:35:42.79	−35:30:50.7	24.258 ± 0.066	23.245 ± 0.019	22.587 ± 0.013	22.362 ± 0.033	22.849 ± 0.108	$5.636^{+0.273}_{-0.262}$
NGFS033546-355921n	03:35:46.30	−35:59:21.4	22.322 ± 0.013	21.393 ± 0.003	20.679 ± 0.003	20.410 ± 0.008	20.973 ± 0.024	$6.405^{+0.290}_{-0.268}$
NGFS033604-352320n	03:36:04.05	−35:23:19.7	23.968 ± 0.060	22.917 ± 0.011	22.191 ± 0.013	⋯	21.973 ± 0.054	$5.759^{+0.370}_{-0.252}$
NGFS033624-355442n	03:36:23.64	−35:54:40.8	24.483 ± 0.086	23.405 ± 0.013	22.664 ± 0.012	22.421 ± 0.048	23.081 ± 0.164	$5.627^{+0.254}_{-0.276}$
NGFS033628-351239n	03:36:27.96	−35:12:38.4	⋯	24.569 ± 0.044	23.847 ± 0.042	23.251 ± 0.090	⋯	$5.340^{+0.433}_{-0.297}$
NGFS033632-362537n	03:36:32.21	−36:25:37.3	⋯	22.419 ± 0.007	21.653 ± 0.006	21.423 ± 0.057	⋯	$6.087^{+0.161}_{-0.159}$
NGFS033637-352309n	03:36:37.27	−35:23:09.1	22.412 ± 0.015	21.366 ± 0.005	20.699 ± 0.0032	20.320 ± 0.006	20.909 ± 0.020	$6.438^{+0.254}_{-0.277}$
NGFS033653-345619n	03:36:53.26	−34:56:18.1	23.056 ± 0.021	21.836 ± 0.005	21.093 ± 0.0038	20.806 ± 0.012	⋯	$6.202^{+0.346}_{-0.255}$
NGFS033657-355011n	03:36:57.12	−35:50:11.4	⋯	25.144 ± 0.060	24.266 ± 0.0491	⋯	⋯	$5.035^{+0.065}_{-0.045}$
NGFS033700-350816n	03:36:59.85	−35:08:15.4	⋯	25.062 ± 0.051	24.563 ± 0.0676	23.917 ± 0.182	⋯	$5.050^{+0.099}_{-0.303}$
NGFS033700-352035n	03:36:59.83	−35:20:36.0	23.493 ± 0.029	22.538 ± 0.007	21.914 ± 0.0065	21.519 ± 0.017	21.984 ± 0.053	$5.918^{+0.318}_{-0.263}$
NGFS033703-354802n	03:37:03.42	−35:48:02.1	⋯	24.784 ± 0.041	23.696 ± 0.0295	22.995 ± 0.073	⋯	$5.461^{+0.139}_{-0.270}$
NGFS033708-344353n	03:37:08.16	−34:43:52.4	24.208 ± 0.067	22.791 ± 0.010	22.121 ± 0.0117	21.655 ± 0.038	21.697 ± 0.091	$5.857^{+0.273}_{-0.274}$
NGFS033710-352312n	03:37:10.04	−35:23:11.8	⋯	24.537 ± 0.090	23.664 ± 0.0386	22.914 ± 0.059	⋯	$5.539^{+0.233}_{-0.282}$
NGFS033710-355317n	03:37:10.35	−35:53:16.9	⋯	25.336 ± 0.072	24.608 ± 0.0793	⋯	⋯	$4.867^{+0.031}_{-0.028}$
NGFS033718-354157n	03:37:17.93	−35:41:57.3	23.708 ± 0.049	22.711 ± 0.010	21.929 ± 0.0082	21.439 ± 0.018	21.835 ± 0.047	$5.972^{+0.336}_{-0.290}$
NGFS033727-355747n	03:37:27.49	−35:57:46.8	⋯	24.945 ± 0.046	25.017 ± 0.0928	⋯	⋯	$5.023^{+0.018}_{-0.020}$
NGFS033734-354945n	03:37:34.04	−35:49:44.9	24.632 ± 0.095	23.451 ± 0.015	22.754 ± 0.0142	22.449 ± 0.048	22.879 ± 0.133	$5.565^{+0.315}_{-0.263}$
NGFS033742-343816n	03:37:41.97	−34:38:15.7	⋯	21.601 ± 0.004	20.961 ± 0.0031	20.670 ± 0.028	⋯	$6.203^{+0.120}_{-0.204}$
NGFS033817-353028n	03:38:16.64	−35:30:27.5	24.332 ± 0.089	23.276 ± 0.017	22.637 ± 0.0145	22.458 ± 0.043	22.588 ± 0.094	$5.586^{+0.274}_{-0.260}$
NGFS033837-355002n	03:38:36.63	−35:50:02.1	⋯	25.875 ± 0.105	24.899 ± 0.0889	22.174 ± 0.034	⋯	$5.671^{+0.349}_{-0.270}$
NGFS033837-355502n	03:38:37.23	−35:55:01.5	⋯	26.191 ± 0.153	25.057 ± 0.1063	22.630 ± 0.057	⋯	$5.440^{+0.370}_{-0.272}$
NGFS033838-354527n	03:38:37.66	−35:45:27.6	23.502 ± 0.031	22.544 ± 0.007	21.866 ± 0.0057	21.346 ± 0.015	22.084 ± 0.058	$5.997^{+0.208}_{-0.287}$
NGFS033845-351600n	03:38:45.40	−35:15:59.6	24.432 ± 0.074	23.578 ± 0.015	22.883 ± 0.0141	22.341 ± 0.038	23.053 ± 0.156	$5.611^{+0.176}_{-0.295}$
NGFS033854-344932n	03:38:54.26	−34:49:32.4	⋯	24.096 ± 0.021	23.307 ± 0.0243	⋯	⋯	$5.377^{+0.016}_{-0.009}$
NGFS033906-360557n	03:39:05.77	−36:05:56.2	22.584 ± 0.018	21.526 ± 0.004	20.786 ± 0.003	20.440 ± 0.008	21.080 ± 0.030	$6.368^{+0.278}_{-0.270}$
NGFS033913-352217n	03:39:13.32	−35:22:16.8	22.080 ± 0.014	21.274 ± 0.005	20.526 ± 0.0037	20.229 ± 0.006	20.775 ± 0.018	$6.486^{+0.269}_{-0.275}$
NGFS033920-354329n	03:39:19.69	−35:43:28.6	22.946 ± 0.024	22.073 ± 0.006	21.356 ± 0.0055	21.036 ± 0.011	21.840 ± 0.045	$6.156^{+0.266}_{-0.275}$
NGFS033950-353122n	03:39:50.08	−35:31:22.1	24.062 ± 0.074	23.256 ± 0.014	22.706 ± 0.015	22.249 ± 0.032	22.985 ± 0.126	$5.640^{+0.289}_{-0.307}$

Table 1
(Continued)

Nucleus	R.A. (J2000) hh:mm:ss.ss	Decl.(J2000) dd:mm:ss.s	u' (AB mag)	g' (AB mag)	i' (AB mag)	J (AB mag)	K_s (AB mag)	$\log(\mathcal{M}_{*,\mathrm{nucleus}})$ ($M_\odot$)
NGFS033955-353943n	03:39:55.44	−35:39:42.9	⋯	25.251 ± 0.063	24.227 ± 0.0465	⋯	⋯	$5.127^{+0.064}_{-0.049}$
NGFS033956-353721n	03:39:56.45	−35:37:20.7	24.124 ± 0.055	23.166 ± 0.011	22.419 ± 0.01	22.106 ± 0.033	22.604 ± 0.090	$5.699^{+0.299}_{-0.266}$
NGFS034001-344323n	03:40:00.56	−34:43:23.3	23.817 ± 0.057	23.103 ± 0.013	22.244 ± 0.011	22.302 ± 0.067	22.264 ± 0.169	$5.798^{+0.214}_{-0.259}$
NGFS034010-355011n	03:40:09.77	−35:50:10.1	⋯	24.234 ± 0.029	23.735 ± 0.03	23.271 ± 0.128	⋯	$5.214^{+0.226}_{-0.247}$
NGFS034019-361850n	03:40:19.35	−36:18:49.9	⋯	24.579 ± 0.033	23.819 ± 0.0315	⋯	⋯	$5.127^{+0.064}_{-0.049}$
NGFS034023-351636n	03:40:23.52	−35:16:35.7	22.556 ± 0.016	21.593 ± 0.004	20.832 ± 0.0028	20.676 ± 0.008	21.187 ± 0.029	$6.380^{+0.215}_{-0.284}$
NGFS034027-362957n	03:40:26.99	−36:29:55.8	⋯	21.709 ± 0.006	20.978 ± 0.0048	⋯	⋯	$6.318^{+0.002}_{-0.002}$
NGFS034031-355241n	03:40:30.65	−35:52:40.7	⋯	-	23.878 ± 0.0505	22.741 ± 0.068	⋯	$5.735^{+0.091}_{-0.272}$
NGFS034034-350122n	03:40:33.83	−35:01:22.3	22.702 ± 0.038	21.597 ± 0.006	20.768 ± 0.0041	20.656 ± 0.011	21.121 ± 0.036	$6.421^{+0.181}_{-0.271}$
NGFS034038-360716n	03:40:37.76	−36:07:16.4	⋯	24.655 ± 0.038	23.903 ± 0.0386	⋯	⋯	$5.127^{+0.064}_{-0.049}$
NGFS034044-361108n	03:40:43.85	−36:11:07.7	⋯	24.081 ± 0.025	23.509 ± 0.0293	23.049 ± 0.191	⋯	$5.235^{+0.153}_{-0.222}$
NGFS034050-354454n	03:40:50.40	−35:44:54.4	20.788 ± 0.005	19.603 ± 0.002	18.718 ± 0.0011	18.389 ± 0.002	18.771 ± 0.003	$7.255^{+0.289}_{-0.261}$
NGFS034101-354434n	03:41:00.78	−35:44:33.2	21.995 ± 0.010	20.959 ± 0.003	20.272 ± 0.0019	19.993 ± 0.007	20.546 ± 0.018	$6.558^{+0.305}_{-0.264}$
NGFS034107-353052n	03:41:07.23	−35:30:51.9	⋯	24.355 ± 0.035	23.706 ± 0.0335	23.204 ± 0.115	⋯	$5.310^{+0.143}_{-0.289}$
NGFS034113-350932n	03:41:12.87	−35:09:31.3	21.879 ± 0.010	20.890 ± 0.003	20.223 ± 0.0024	20.212 ± 0.010	20.674 ± 0.029	$6.490^{+0.081}_{-0.015}$
NGFS034135-352625n	03:41:35.06	−35:26:24.3	⋯	23.736 ± 0.018	22.882 ± 0.0143	⋯	⋯	$6.318^{+0.002}_{-0.002}$
NGFS034217-353227n	03:42:17.25	−35:32:26.6	⋯	20.562 ± 0.003	19.801 ± 0.0018	⋯	⋯	$6.780^{+0.001}_{-0.001}$
NGFS034218-352819n	03:42:17.83	−35:28:18.7	⋯	25.447 ± 0.082	24.545 ± 0.0717	⋯	⋯	$4.938^{+0.076}_{-0.069}$
NGFS034225-353541n	03:42:25.22	−35:35:41.5	⋯	24.208 ± 0.024	23.421 ± 0.0212	⋯	⋯	$5.127^{+0.064}_{-0.049}$

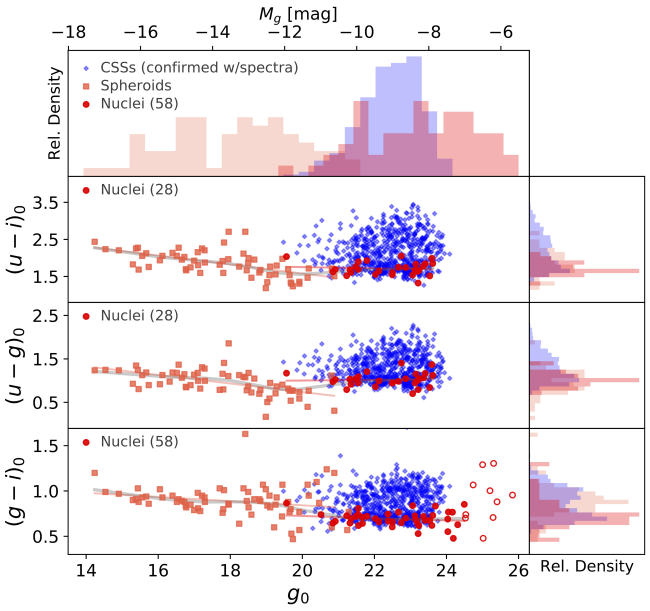

Figure 5. Color–magnitude diagrams for the NGFS sample nuclei shown as red circles. Blue diamonds are CSSs that were confirmed by radial velocities, taken from Wittmann et al. (2016), and orange squares mark the spheroid colors and luminosities of the host dwarf galaxies in which the nuclei of our sample were found. Linear relations show the weighted least-squares fits to the nuclei and spheroid color–magnitude relations (see text for details), while the gray curve is a LOWESS fit to the combined nuclei+spheroid sample.

galaxies: $A_u = 0.056$, $A_g = 0.043$, $A_i = 0.022$, $A_J = 0.009$, $A_{K_s} = 0.004$.

4. Results

4.1. Color–Magnitude and Color–Color Diagrams

Figure 5 illustrates the color–magnitude diagrams (CMDs) in the filter combinations $(u'-i')_0$, $(u'-g')_0$, and $(g'-i')$ versus g'_0. The nuclei of this work are shown as red circles and their host galaxy spheroid components as orange squares. For comparison, we also plot radial-velocity-confirmed compact stellar systems (CSSs, i.e., GCs and ultracompact dwarfs or UCDs) near the cD galaxy NGC 1399 from the clean compilation catalog in Wittmann et al. (2016) as blue symbols.

The nuclei occupy the bluest parts of the CSS distribution in all three colors with mean values $\langle(u'-i')_{0,\rm nuc}\rangle = 1.71 \pm 0.03$, $\langle(u'-g')_{0,\rm nuc}\rangle = 1.02 \pm 0.03$, and $\langle(g'-i')_{0,\rm nuc}\rangle = 0.73 \pm 0.03$, compared to CSSs that cover a significantly broader range of colors with mean values $\langle(u'-i')_{0,\rm CSSs}\rangle = 2.15 \pm 0.02$, $\langle(u'-g')_{0,\rm CSSs}\rangle = 1.28 \pm 0.01$, and $\langle(g'-i')_{0,\rm CSSs}\rangle = 0.87 \pm 0.01$. The broader distribution for CSSs and their extension to redder colors are mainly due to their larger spread in metal content reaching supersolar values (e.g., Kissler-Patig et al. 1998). On the other hand, both samples have similar luminosity distributions. One of the key findings here is that the NGFS nuclei show a flat color–magnitude relation (CMR). Whether this is due to no significant changes in the stellar population content as a function of stellar mass will be discussed below. We point out that this is opposite to other results from studies focused on nuclei in the brighter nucleated dwarf galaxy regime, where a CMR for nuclei was found in the magnitude range $-16 \gtrsim M_B \gtrsim -18$ mag, while for nucleated galaxies brighter than $M_B \simeq -18$ mag, the relation becomes flatter again (Côté et al. 2006; Turner et al. 2012; Spengler et al. 2017).

Table 2
Nucleus and Spheroid Color–Magnitude Relations

Linear wLSQ Fits	r	p	σ
$(u'-i')_{\rm nuc} = -0.017\,g' + 2.094$	−0.103	0.602	0.032
$(u'-i')_{\rm sph} = -0.121\,g' + 4.008$	−0.582	$8.511 \cdot 10^{-7}$	0.022
$(u'-g')_{\rm nuc} = +0.008\,g' + 0.848$	+0.050	0.800	0.030
$(u'-g')_{\rm sph} = -0.098\,g' + 2.704$	−0.560	$2.744 \cdot 10^{-6}$	0.019
$(g'-i')_{\rm nuc} = -0.012\,g' + 0.969$	−0.175	0.267	0.011
$(g'-i')_{\rm sph} = -0.023\,g' + 1.303$	−0.229	0.076	0.013

Note. The left column shows the weighted least-squares fits for nuclei and spheroids in various filter combinations (see Figure 5), the second column gives the correlation coefficient (r), and the next the p value for the hypothesis that the CMR has zero slope, while the last column is the standard error of the gradient. The relations for the spheroids are valid in the range $-18 \lesssim g' \lesssim -10.5$, while the corresponding relations for the nuclei are valid in the range $-11 \lesssim g' \lesssim -7.5$ mag.

In comparison to the nuclei, the spheroid components of their host galaxies show a shallow but measurable CMR, with the spheroid colors becoming redder for brighter systems. Table 2 summarizes the numerical properties of the weighted linear least-squares fits to the CMR of nuclei and spheroids in various filter combinations. The CMR of the red-sequence galaxies (including dwarfs) in Virgo and Fornax was recently shown to become flatter going from the brightest galaxies toward the faint dwarf luminosity regime (Roediger et al. 2017; Eigenthaler et al. 2018). The CMR is usually interpreted as a mass–metallicity relation (MZR) due to deeper potential wells retaining more metals produced by stars during the secular evolution of the galaxy compared to their less massive counterparts (e.g., Kodama & Arimoto 1997; Tremonti et al. 2004; Kewley & Ellison 2008; Torrey et al. 2017, and references therein). In relation to the flat CMR of the nuclei, we find at the overlap luminosity of $M_{g'} \simeq -11.0$ mag an offset of $\delta(u'-i')_0 \approx 0.2$ and $\delta(u'-g')_0 \approx 0.31$, but a relatively small offset in the optical color of $\delta(g'-i')_0 \approx 0.13$. These color offsets have implications for the differences in stellar population contents between nuclei and the surrounding galaxy spheroids and provide constraints for the formation mechanisms of galaxy nuclei and the build-up of galaxies and CSSs in galaxy clusters. We will come back to this point in the discussion section.

Figure 6 shows two color–color diagrams, that is, $(u'-g')_0$ versus $(g'-i')_0$ or $u'g'i'$ (top panel) and $(u'-i')_0$ versus $(i'-K_s)_0$ or $u'i'K_s$ (bottom panel), where gray dots represent all of the detected NGFS sources for which PSF-based photometry could be obtained in the central region of Fornax (Figure 1). These color–color diagrams, in particular the $u'i'K_s$ plane with its broad SED coverage, are powerful tools to distinguish among different object types, such as foreground stars, background galaxies, and CSSs (Muñoz et al. 2014). The upper left cloud of objects in both diagrams shows the location of redshifted background galaxies, while in the lower parts of the $u'g'i'$ diagram, a tight sequence holds for individual foreground stars and star clusters, but in the $u'i'K_s$ diagram even these objects are separated into two sequences. Here the central sequence marks the star cluster sequence, as it is shown by the confirmed CSSs (blue symbols) from the very central parts of the Fornax cluster. Our nuclei sample (red solid

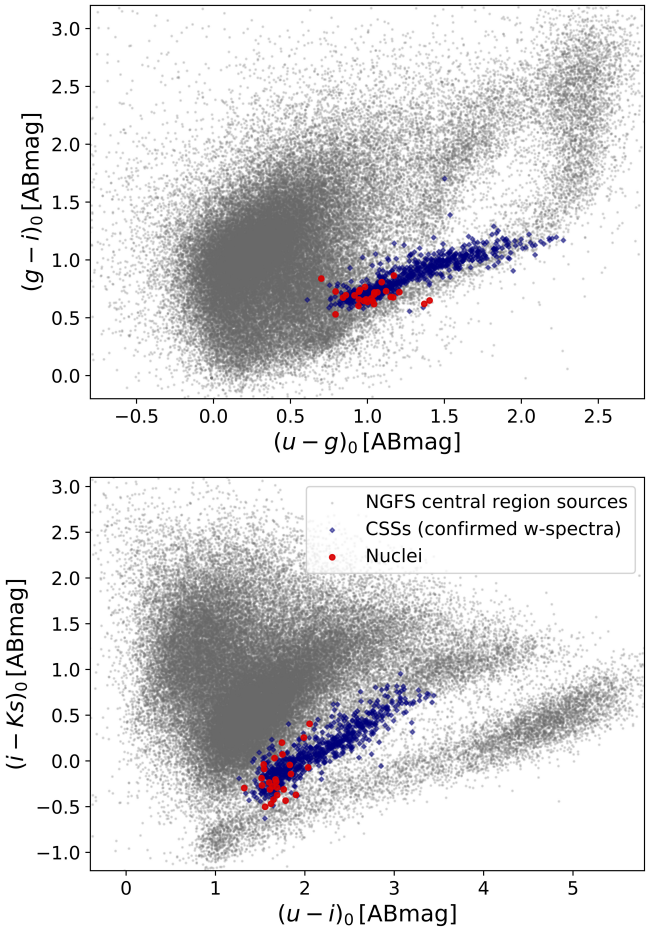

Figure 6. Color–color diagrams, $(u'-g')_0$ vs. $(g'-i')_0$ (top panel) and $(u'-i')_0$ vs. $(i'-K_s)_0$ (bottom panel), showing as gray dots all of the NGFS central sources in the $R < R_{\rm vir}/4$ with PSF photometry. The red solid circles represent the nuclei of this work, and the blue diamonds show the confirmed CSSs in the surroundings of the cD galaxy NGC 1399. Compact stellar systems such as GCs, UCDs, and nuclei lie in a very narrow region in color–color space, which makes the $u'\,g'i'$ and $u'i'K_s$ diagrams very powerful tools to select CSS candidates.

circles) is located in the same color–color region and confined to the bluest parts of the star cluster sequence, as was already seen in the color–magnitude diagrams (see Figure 5). The analysis of the complete star-cluster photometry catalog in the central Fornax region with the new GC and UCD candidates will be reported in a future work. In the subsequent analysis we focus on the dwarf galaxy nuclei.

4.2. Stellar Mass Estimates

Stellar masses for our NGFS nuclei are estimated using a χ^2 minimization approach to fit stellar population synthesis models to the photometric information from the NGFS filters $g'i'JK_s$, $g'i'J'$, or $g'i'$, according to the photometry available for each nucleus. We exclude the u'-band photometry due to its sensitivity to very young stellar populations with low mass fractions or potential active galactic nucleus emission components, if any. The mass errors are estimated with Monte Carlo simulations by drawing 1000 random values from a normal probability distribution function with a mean corresponding to the observed magnitude and a standard deviation equal to the magnitude error, and propagating these values through the following calculations. Simple stellar population models from

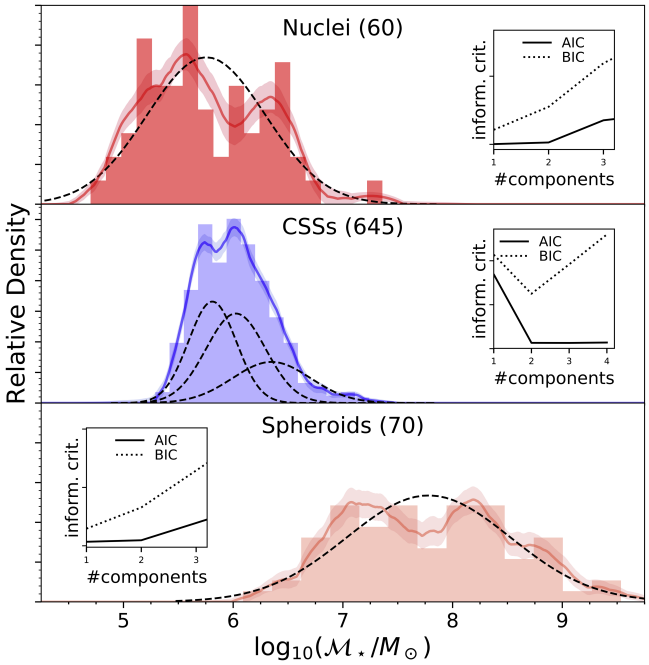

Figure 7. Mass distribution for the NGFS nuclei (top panel), the radial-velocity-confirmed CSSs in Fornax (middle panel), and the dwarf spheroids (bottom panel). The probability density distribution for each sample is overplotted using an Epanechnikov kernel density estimate together with the 1σ uncertainty ranges. The size of each sample is given in parentheses in the corresponding panel. The inset figures show the Aikake and Schwarz (Bayesian) information criteria (AIC and BIC; see Ivezić et al. 2014), which define the most likely number of Gaussian components for each distribution; here we use the AIC. The corresponding Gaussians are indicated by the dashed curves.

Bruzual & Charlot (2003, hereafter BC03) with the 2016 update,[17] the MILES atlas (Sánchez-Blázquez et al. 2006), and an initial mass function (IMF) from Kroupa (2001) are used to estimate luminosity-weighted stellar masses. We consider metallicities in the range $0.0001 \leqslant Z/Z_\odot \leqslant 0.5$ and ages older than 1 Gyr to avoid the stochasticity typically found at younger ages (e.g., Cerviño et al. 2002; Cerviño & Luridiana 2004; Fouesneau & Lançon 2010). The stellar mass distribution of our nuclei covers the range $\log(\mathcal{M}_\star/M_\odot) = 4.8$–$7.3$ with uncertainties ranging from ∼8% to 43% and a mean uncertainty of ∼19%, propagated from the photometric errors. We point out that there are systematic uncertainties of the mass estimates related to the choice of population synthesis models and the set of filters used to compute the mass-to-light conversion (see Powalka et al. 2016a, 2017; Zhang et al. 2017), which for our sample we estimate to be at most ∼0.2 dex.

The stellar mass distribution for the NGFS nuclei is illustrated in Figure 7, together with the distribution of the confirmed CSSs in the Fornax region, for which we estimate their masses with the same procedure applied to our nuclei, as well as the nucleated NGFS dwarf spheroids,[18] for which we use the mass measurements estimated in Eigenthaler et al. (2018), which are based on the parameterizations of the mass-to-light ratios as a function of various colors given in Bell et al. (2003). We point out that our sample dwarf spheroids do not show any signs of star formation activity, and, hence, their

[17] http://www.bruzual.org/~gbruzual/bc03/Updated_version_2016/

[18] Note that we consider the spheroid mass alone; the nucleated spheroid mass does not include the nucleus.

optical colors serve as good indicators for their stellar masses (see Zhang et al. 2017 for the numerical accuracy of these conversions). An Epanechnikov kernel probability density estimate (KDE) is overplotted for each distribution together with its 1σ uncertainties.

We observe that the mass distributions for the three populations are quite different morphologically and cover different mass ranges. At the low-mass end, this is due to differences in the respective selection functions. The NGFS nuclei sample reaches lower masses than the CSS sample, because the spectroscopic selection function for the radial-velocity confirmation of CSSs in Fornax has a brighter cutoff (Wittmann et al. 2016) than the NGFS point-source detection limit (see Section 3.1). The mass distribution of dwarf spheroids is limited at the lower-mass end by the surface-brightness detection limit of these systems (see Eigenthaler et al. 2018). The nuclei population spans more than two orders of magnitude in stellar mass and shows a bimodal distribution, for which the peaks are located at $\log(\mathcal{M}_\star/M_\odot) \simeq 5.38$ and $\sim$6.25; the latter value is consistent with ultracompact dwarf (UCD) masses (e.g., Misgeld & Hilker 2011). Although the AIC marginally prefers one over two components, the Epanechnikov density distribution favors two components. We find that the CSS distribution is formally trimodal[19] with its peaks located at $\log(\mathcal{M}_\star/M_\odot) \simeq 5.81$, 6.02 and $\sim$6.35, with the last component extending toward higher masses, reminiscent of UCDs as well. We will not discuss this interesting feature of the Fornax globular cluster mass function in this work, as it requires an in-depth analysis of the sample selection function, but keep our focus on the dwarf galaxy spheroids and nuclei. The dwarf spheroid mass distribution occupies a broad range of more than three magnitudes with a mild but statistically nonsignificant bimodality ($\log[\mathcal{M}_\star/M_\odot] \simeq 7.25$ and $\sim$8.25), with its single Gaussian peak at $\log(\mathcal{M}_\star/M_\odot) \simeq 7.8$. To our knowledge, this is the first time such hints of multimodalities in the nucleated spheroid mass and the nucleus mass distribution have been detected. Together they may give us hints at the importance of different formation mechanisms of stellar nuclei.

4.3. Stellar Population Properties

Color information in combination with population synthesis model predictions can be used to understand the stellar population properties of the nuclei, such as age, metallicity, and correlations with their mass. The $u'i'K_s$ diagram helps minimize the age–metallicity degeneracy that affects broad-band filters. Figure 8 illustrates the $u'i'K_s$ diagram with overplotted SSP models from BC03, showing isometallicity tracks for the range $0.0001 < Z < 0.05$ with equivalent ages of 1, 2, 5, and 13.8 Gyr. Solid circles stand for NGFS nuclei color coded by their stellar masses. As in the previous figures, radial-velocity-confirmed CSSs are shown for comparison purposes. We observe that the NGFS nuclei occupy approximately the bluer half of the CSSs $u'i'K_s$ spread, which is consistent with subsolar metallicities ($Z < Z_\odot$) or a young stellar age component. This is in line with the measurements of Paudel et al. (2011), who find from spectroscopy of relatively bright Virgo dwarf galaxies ($-18.5 \gtrsim M_{r,\mathrm{gal}} \gtrsim -15.5$) that their nuclei ($-13.3 \gtrsim M_{r,\mathrm{nuc}} \gtrsim -10.2$) cover a large range of metallicities from slightly supersolar (+0.18 dex) to significantly subsolar (−1.22 dex) values. However, it is still challenging to disentangle ages and metallicities for stellar systems older than a few gigayears at any metallicity based on photometry alone. The inversion of broadband color information into stellar population parameters is notoriously difficult (Hansson et al. 2012; Powalka et al. 2016a, 2017) and is facing limitations in light of potentially yet to be understood systematics related to the galaxy cluster environment (Powalka et al. 2016b). Given the previous considerations, we refrain from assigning numerical age and metallicity values to the nuclei, but analyze them in groups.

4.3.1. Bimodality in Nucleus Stellar Population Properties

Although there is no clear mass–color relation, the mass bimodality of our NGFS nuclei is seen as mainly two groups in the $u'i'K_s$ plane, hereafter referred to as groups $\mathcal{A}$ and $\mathcal{B}$, and indicates a bimodality in their stellar population parameters. The nuclei in group $\mathcal{A}$ have stellar masses $\gtrsim 10^6\,M_\odot$ and lie in the bluest color–color region of the $u'i'K_s$ plane with $(u'-i')_0 < 2.0$ mag and $(i'-K_s)_0 < -0.2$ mag. Nuclei in group $\mathcal{B}$ cover a more extended $u'i'K_s$ color space with redder average colors, $(i'-K_s)_0 \gtrsim -0.2$ mag, and comprise objects with stellar masses $\lesssim 10^6\,M_\odot$.[20] The mean masses for the groups are close to the masses of the two peaks in the nuclei stellar mass distribution, but it is worth noticing that from the total sample, 26 nuclei have high-quality $u'i'K_s$ photometry to robustly estimate their color–color distribution. This is mainly the reason for the slightly different peaks between the bimodal mass distribution and the mean masses of the two groups considered here. In any case, it is clear that according to the nucleus mass distribution from Figure 7, there is a bimodality of nuclei that is also reflected in the $u'i'K_s$ diagram and that bimodality correlates with stellar population parameters specific for two nuclei subgroups.

Assuming SSP-like stellar populations, we observe that our NGFS nuclei in group $\mathcal{A}$ host very metal-poor stellar populations ($Z < 0.0004 = 0.02\,Z_\odot$) with luminosity-weighted ages older than $\sim$2 Gyr. In contrast, the nuclei in group $\mathcal{B}$ show colors equivalent to metallicities in the range $0.004 < Z < 0.02$ ($0.2 < Z/Z_\odot < 1$) and ages younger than $\sim$2 Gyr. The reddening vector in Figure 8 illustrates how an intrinsic reddening of $A_V = 0.5$ mag, equivalent to $E_{B-V} = 0.16$ for a Milky Way reddening curve, would affect the $u'i'K_s$ color–color space. The reddening direction points toward increasing metallicity values, but does not affect the age significantly—if anything, it pushes the colors toward older equivalent ages. Alternatively, chemical abundance ratios different from the ones assumed in the solar-scaled BC03 models may bias the age and metallicity estimates. Evidence that this is indeed the case comes from the study of Paudel et al. (2010), who found supersolar [α/Fe] ratios in nuclei of Virgo dwarfs. In their photometric study of compact stellar systems in the Virgo cluster, Powalka et al. (2016b) found intriguing offsets in multicolor relations pointing toward younger ages of some Virgo GCs. Although tests showed the influence of increased

[19] We point out that the AIC has a minimum of three components, but the AIC for two components is numerically very close to the formal minimum. In addition, the BIC gives two as the most likely number of components, which indicates that bimodality and trimodality are equally likely representations of the CSS mass distribution.

[20] One exception in group $\mathcal{A}$ is the massive nucleus in the center of dwarf NGFS034050-354454 with a stellar mass of $\log(\mathcal{M}_\star/M_\odot) \simeq 7.26$ and colors consistent with $Z \simeq 0.004$ and $\sim$3 Gyr (yellow symbol in Figure 8).

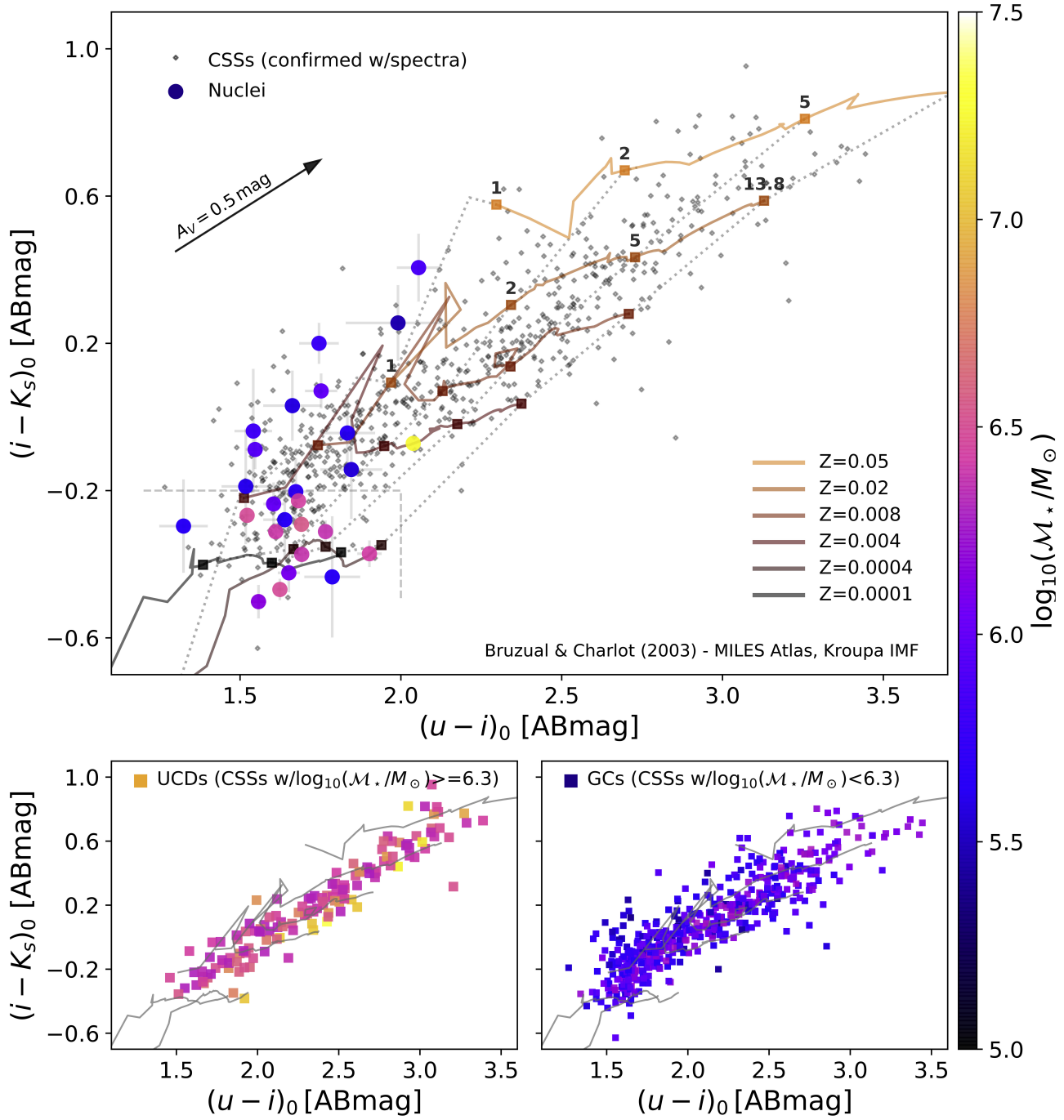

Figure 8. Top panel: $(u' - i)_0$ vs. $(i' - K_s)_0$ color–color diagram with SSP models from BC03 using the MILES stellar library and a Kroupa IMF. Isometallicity tracks are shown as solid lines, ranging from $Z = 0.0001$ to 0.05 (see legend). Squares mark ages of 1, 2, 5, and 13.8 Gyr on each isometallicity track (see labels on the $Z = 0.05$ and $Z_\odot$ track). These points are connected by dotted iso-age lines. Nuclei are color coded using their stellar masses as indicated by the color bar. The arrow in the top left corner shows a reddening vector of $A_V = 0.5$ mag. Bottom panels: the left and right panels indicate the color–color relations of UCDs and GCs, respectively. Their stellar masses are color coded on the same scale as for the top panel. GC stellar masses range from $10^{5.4}$ to $10^{6.3}$ $M_\odot$. UCD stellar masses range from $10^{6.3}$ to $10^{7.5}$ $M_\odot$.

[α/Fe] on colors, the team found that typical α-element enhancements of Local Group GCs were producing too-small color offsets to match the observations at old ages. We, therefore, tentatively conclude that the younger ages of the nuclei in group $\mathcal{B}$ are not primarily due to intrinsic reddening and [α/Fe] variations, but likely are due to genuinely younger and more metal-rich stellar populations, which lie in terms of stellar mass in the low-mass mode of the nucleus stellar mass bimodality. Overall, these results point to different formation histories and perhaps different mechanisms of nucleus formation between the two groups. We will come back to this in the Discussion.

4.3.2. Comparison of Nuclei with Confirmed UCDs

The nuclei masses are shown in color code in the $u'i'K_s$ color–color diagram in Figure 8 (top panel) and are compared to the corresponding stellar mass distribution of radial-velocity-confirmed CSSs in Fornax (bottom panels). From this CSS sample, UCDs are selected with a stellar mass cut so that

$\log \mathcal{M}_\star/M_\odot(\mathrm{UCD}) \geqslant 6.3$ (e.g., Taylor et al. 2010; Mieske et al. 2013), avoiding any restriction in color (i.e., metallicity), while GCs are selected with $\log \mathcal{M}_\star/M_\odot(\mathrm{GC}) < 6.3$ from the same parent CSS sample. The final UCD sample exhibits stellar masses within the range $\log(\mathcal{M}_\star/M_\odot) = 6.3$–$7.4$, whereas the GCs cover the mass range $\log(\mathcal{M}_\star/M_\odot) = 5.4$–$6.3$, which is limited at the low-mass end by the spectroscopic selection function of the CSS sample (Wittmann et al. 2016). The majority of our NGFS nuclei are less massive than $\log(\mathcal{M}_\star/M_\odot) \simeq 6.8$, with the exception of three objects with a stellar mass of $\log(\mathcal{M}_\star/M_\odot) \simeq 7.2$–$7.3$ (see Figure 7), only one of which has a $u'i'K_s$ color and is plotted in Figure 8.

Comparing the stellar masses and stellar population parameters of nuclei with those of UCDs reveals that the members of the low-mass mode of our sample nuclei cannot be the progenitors of Fornax UCDs. These dwarf nuclei have simply too-low masses to be considered a parental population. However, nuclei that are members of the high-mass mode could potentially be considered progenitors of metal-poor Fornax UCDs. Considering that the initial mass of UCD progenitors may be even higher than their current mass and given their likely mass evolution, as suggested in some UCD formation scenarios that involve stripping (e.g., Zinnecker et al. 1988; Bassino et al. 1994; Bekki et al. 2001, 2003; Goerdt et al. 2008; Pfeffer & Baumgardt 2013), even this evolutionary connection may be questionable given the similar present-day masses of high-mass dwarf nuclei and metal-poor UCDs. This may not be the case for the most massive dwarf nucleus in our sample, NGFS034050-354454n, which qualifies as a potential intermediate-metallicity Fornax UCD seed, even after 90% of its present-day mass is lost. In any case, our data suggest that the progenitors of the massive, metal-rich UCDs in Fornax have long been destroyed and have no present-day counterparts in dwarf galaxy nuclei. This is consistent with previous spectroscopic studies (Evstigneeva et al. 2007; Francis et al. 2012).

4.3.3. Comparison of Nuclei with Confirmed GCs

The picture is different when we compare the properties of nuclei and GCs. Essentially all of our nuclei can be considered potential future GCs, once the spheroid envelopes surrounding them are stripped during their dynamical evolution within the Fornax cluster (Bekki et al. 2003; Goerdt et al. 2008; Smith et al. 2013, 2015). Such potential nuclei remnants may become future members of the Fornax GC system. The younger stellar ages of the low-mass-mode nuclei indicate extended star formation histories and, therefore, prolonged chemical enrichment processes that may lead to significant abundance spreads, especially in Fe-peak elements. Such future GCs could be clearly identified with the next generation of 30 m class telescopes via their spreads in stellar iron abundances, something that has been measured in numerous Milky Way star clusters (e.g., Willman & Strader 2012). Alternatively, high-spatial-resolution imaging allows one to identify remnant nuclei candidates in the half-light radius versus luminosity parameter space, which has been done for the Local Group star clusters (Ma et al. 2006). Furthermore, the characteristic age–metallicity relation found for a subset of Galactic GCs (Leaman et al. 2013; VandenBerg et al. 2013) is consistent with our observation of decreasing stellar ages in more metal-rich nuclei. This suggests that at least the Galactic GC subpopulation with a significant age–metallicity relation could have in part their origins in the cores of nucleated dwarf galaxies (see also Marín-Franch et al. 2009; Forbes & Bridges 2010; Dotter et al. 2011; de Boer et al. 2015).

4.4. Differences between Nuclei and Galaxy Spheroids

The color difference in various filter combinations between the nucleus and its host galaxy spheroid is shown in Figure 9 as a function of nucleus luminosity ($g_{0,\mathrm{nuc}}$) and galaxy spheroid luminosity ($g_{0,\mathrm{sph}}$). The nucleus-to-galaxy mass ratio is encoded by the symbol color and has a range from 0.1% to 10%. The color differences are more correlated with the spheroid light than with the nucleus luminosity, which implies that the mechanisms that lead to the color offsets must be acting more on galaxy scales rather than nucleus scales. One can think of processes that are correlated with the total dwarf galaxy mass that, for instance, lead to more massive galaxies holding on more efficiently and longer to their gas supply than their small-mass counterparts; this is especially true in the galaxy cluster environment.

We find relations for the color differences $\Delta(u'-i')_0$ and $\Delta(u'-g')_0$ versus $g_{0,\mathrm{nuc}}$ and $g_{0,\mathrm{sph}}$. These near-UV+optical colors map a broader SED range that is more sensitive to changes in stellar population parameters, while a shallower trend in $\Delta(g'-i')_0$ is consistent with the narrower SED coverage. This is mainly due to the enhanced sensitivity of the u band to the Balmer break flux compared to the redder filters. Bright nuclei ($M_{g,\mathrm{nuc}} \lesssim -10$), on average $\Delta(u'-i')_0 = -0.35$, $\Delta(u'-g')_0 = -0.15$, and $\Delta(g'-i')_0 = -0.2$ mag bluer than their host galaxy, are indicative of younger or more metal-poor stellar populations (see Figure 8). According to the BC03 models, these color differences correspond consistently to an age difference of $\Delta t/t \simeq -0.8$ at old absolute ages ($\sim$13 Gyr) and low metallicities $Z = 0.0001$–0.004 ([Fe/H] $\simeq -2.3$ to -1.6 dex), and an age difference of $\Delta t/t \simeq -0.5$ at young absolute ages ($\sim$2 Gyr) and solar metallicities. The difference can also be attributed to a metallicity difference of Δ[Fe/H] ≈ -1 dex at old absolute ages ($\sim$13 Gyr) and intermediate to low metallicities ([Fe/H] $\simeq -0.5$ to -1.6 dex) and to Δ[Fe/H] ≈ -0.3 dex at solar metallicities, respectively. These metallicity differences change at young absolute ages ($\sim$2 Gyr) to Δ[Fe/H] ≈ -1.3 dex at intermediate to low metallicities and Δ[Fe/H] ≈ -0.6 dex at solar metallicities, respectively. Similar color differences have been reported in previous studies (see Lotz et al. 2004; Côté et al. 2006; Turner et al. 2012). However, owing to the depth of the present data, we find that there is a transition point around $g_{0,\mathrm{nuc}} \approx 24$ mag ($M_{g,\mathrm{nuc}} \approx -7.5$) or $g_{0,\mathrm{sph}} \approx 19$ mag ($M_{g,\mathrm{sph}} \approx -12.5$) where the average $(g'-i')_0$ offset becomes insignificant at the expense of an increasing galaxy-to-nucleus color variance. This feature is noticeable in $(u'-i')_0$ and $(u'-g')_0$ colors already at brighter nucleus luminosities around $g_{0,\mathrm{nuc}} \approx 22$ mag ($M_{g,\mathrm{nuc}} \approx -9.5$) or $g_{0,\mathrm{sph}} \approx 17.5$ mag ($M_{g,\mathrm{sph}} \approx -14$).

Another important feature is the steep relation seen in the $\Delta(u'-i')_0$ and $\Delta(u'-g')_0$ colors versus $g_{0,\mathrm{sph}}$: here we observe that low nucleus-to-galaxy mass ratios (<2%) only occur up to a magnitude $g_{0,\mathrm{sph}} \approx 17.5$ mag ($M_{g,\mathrm{sph}} \approx -14$), where we find almost exclusively blue nuclei, while for fainter dwarfs we have a mixture of nucleus-to-galaxy color differences and nucleus-to-galaxy mass ratios. We note that all of the trends described here are not due to photometric uncertainties but to stellar population properties that vary substantially from nucleus to nucleus.

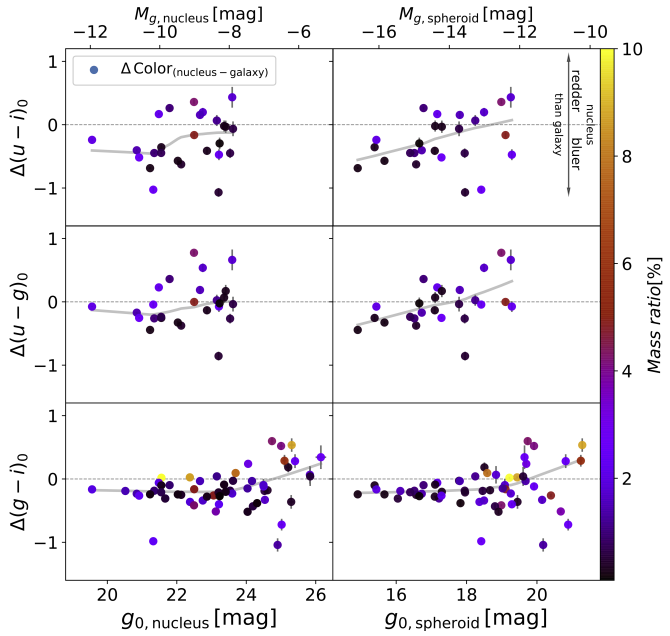

Figure 9. Color differences between the nucleus and its host dwarf galaxy spheroid in $\Delta(u'-i')_0$, $\Delta(u'-g')_0$, and $\Delta(g'-i')_0$ (top to bottom panels) vs. $g_{0,\mathrm{nucleus}}$ (right panels) and vs. $g_{0,\mathrm{spheroid}}$ (left panels). The color code of the symbols shows the corresponding nucleus-to-galaxy mass ratio encoded by the vertical color bar. The gray curves represent LOWESS fits to the data. The arrows in the top panel show the directions in which the nucleus becomes redder or bluer than its host galaxy. Note that photometric errors are for most data points smaller than the symbol size.

These results paint the following picture: as a dwarf nucleus begins to grow, starting with a low nucleus-to-galaxy mass ratio, its stellar population content is dominated by more metal-poor or younger stars than the typical star in its host spheroid. Nuclei with higher nucleus-to-galaxy mass ratios must have either reached higher metal enrichment at similar ages or were formed earlier with enough time for their stellar populations to evolve and redden sufficiently. A distinction between these two scenarios could easily be made using spectroscopically determined [α/Fe] ratios, which are indicators of star formation timescales (e.g., Matteucci & Greggio 1986), allowing us to discern between prolonged star formation histories versus short and early star formation bursts (e.g., Tsujimoto et al. 1995; Matteucci & Recchi 2001), which may be driven by the environment (e.g., Puzia et al. 2005; Thomas et al. 2005).

5. Discussion

5.1. Formation Mechanisms

The astrophysical mechanisms responsible for the differences in stellar population content of the galaxy spheroid and the nucleus are numerous, but can be categorized to be mainly due to two processes: (1) the inflow of gas into the nuclear regions, which triggers star formation processes (e.g., van den Bergh 1986; Antonini et al. 2015), and (2) the accretion of GCs into the galaxy central regions via dynamical friction (e.g., Tremaine et al. 1975; Lotz et al. 2001; Arca-Sedda & Capuzzo-Dolcetta 2014). However, the relatively shallow dwarf galaxy potentials can be easily affected by environmental and secular processes. Secular processes such as stellar winds, supernova (SN), and black hole (BH) feedback can affect the nucleus formation and evolution, for instance, by helping with gas supply to the nuclear regions through stellar winds from newly formed stars (radiation drag, Kawakatu & Umemura 2002), or slowing down the nucleus growth due to SN-driven winds contributing to the mass loss in dwarf galaxies and likely changing the dynamical friction timescales for orbiting star clusters to sink to the center (Lotz et al. 2001), or dynamically heating the nuclear cluster due to a massive central BH (Antonini et al. 2015). Whether the gas comes from disk instabilities, galaxy mergers (with some gas content), or primordial gas, the dynamical timescales for the gas to sink down to the nuclear reservoir depend on the size of the galaxy, being longer with increasing galaxy size and, thus, mass (Eigenthaler et al. 2018). Therefore, in more massive galaxies, the inflowing material would have more time to fragment and undergo star formation, leaving smoother and relatively steeper stellar population gradients imprinted in the spheroid component. Consequently, the spheroids of low-mass dwarfs would have smaller and more stochastic population gradients due to gas or GCs having shorter sink-in timescales, leading to a more stochastic color difference between nucleus and host galaxy than for more massive dwarfs. This is exactly what we observe in Figure 9 for $M_{g,\mathrm{sph}} \leqslant -14$ and $M_{g,\mathrm{nuc}} \leqslant -9.5$ mag.

5.2. Scaling Relations

One of the physical scaling relations that nuclei follow is the nucleus-to-galaxy mass relation (see Figure 10), which has been shown to hold for bright ETGs (e.g., Spengler et al. 2017). To test whether such a relation applies to our dwarf galaxy sample, we use the masses derived for the nuclei in this work (Section 4.2) and their spheroid masses from Eigenthaler et al. (2018). In order to compare our sample with nucleated galaxies at higher masses and those located in different environments, we make use of literature data. For the bright nucleated galaxies in the Fornax cluster sample from ACSFCS (Turner et al. 2012), the corresponding nucleus masses are estimated with the same method described in Section 4.2 using their g, z photometry. For their host galaxies, the B, V magnitudes were obtained from HyperLEDA, and together with the relations from Bell et al. (2003), we estimate the masses in a self-consistent procedure as for the NGFS dwarf galaxies (Eigenthaler et al. 2018). For the Virgo cluster, we use the masses estimated in the Virgo Redux work (Spengler et al. 2017) for nuclei and hosts. In addition, we include the results of recent studies by Nguyen et al. (2017, 2018) for field ETGs to estimate the dynamical mass for their central BH and their nuclear star cluster. In Nguyen et al. (2017), the central SMBH dynamical mass for NGC 404 was estimated to be $1.5 \times 10^5\,M_\odot$. In Nguyen et al. (2018), four field ETGs were studied. Three of them were found to contain BHs with masses of $2.5 \times 10^6\,M_\odot$ (M32), $8.8 \times 10^5\,M_\odot$ (NGC 5102), and $4.7 \times 10^5\,M_\odot$ (NGC 5206). The catalog of nucleated LTGs comes from Georgiev et al. (2016) with 228 moderately inclined spiral galaxies with morphological type code $T \geqslant 3$ or later than Sb at distances $<$40 Mpc. Nuclei from Local Volume (LV) dwarf irregular (dIrr) and early-type dwarf galaxies come from Georgiev et al. (2009). For the Milky Way and Andromeda nuclear star clusters, we use $\mathcal{M}_{\mathrm{MW,NSC}} = (2.5 \pm 0.4) \times 10^7 M_\odot$ from Schödel et al. (2014) and $\mathcal{M}_{\mathrm{M31,NSC}} = (3.5 \pm 0.8) \times 10^7 M_\odot$ from Kormendy & Ho (2013).

The relation between nucleus and host galaxy stellar mass is shown in Figure 10 (top panel), where we see a clear mass

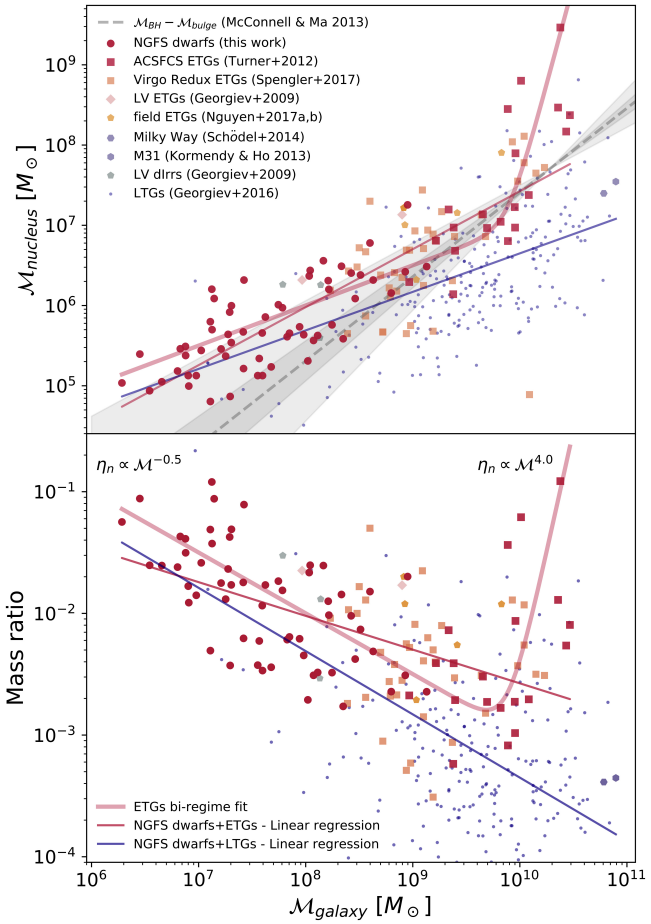

Figure 10. Top panel: nucleus vs. host galaxy stellar mass for different subsets of nucleated NGFS galaxies and other galaxies from the literature. The SMBH mass vs. galaxy mass relation from McConnell & Ma (2013) is shown with 1σ and 3σ limits as dashed-line and shaded regions, respectively. Bottom panel: nucleus-to-galaxy mass ratio ($\eta_n = \mathcal{M}_{\rm nuc}/\mathcal{M}_{\rm gal}$) vs. galaxy mass. We approximate the ETG data with a bi-regime fit for which the slopes of the low-mass and high-mass galaxy masses are labeled.

correlation between nuclei and their host galaxies across the entire galaxy mass range ($6 \lesssim \log[\mathcal{M}_*/M_\odot] \lesssim 11$). For ETGs, this relation is shallower for lower-mass galaxies compared to the massive galaxy regime with a break in slope around $\log(\mathcal{M}_*/M_\odot) \simeq 9.7$. The relation for dwarf galaxies scales as $\eta_n \propto \mathcal{M}_{\rm gal}^{-0.5}$, while for massive ellipticals it follows a much steeper relation, $\eta_n \propto \mathcal{M}_{\rm gal}^{4}$. The discussion of the astrophysical reasons for these two regimes goes far beyond the scope of this paper.

Compared to ETGs, there is a higher dispersion and a less inclined slope for the LTG relation, which is more noticeable in the massive galaxy range, as was already pointed out by Georgiev et al. (2016). This indicates that the nuclei in LTGs are on average less massive at a fixed host galaxy mass than nuclei in ETGs. The weighted linear and polynomial least-squares fits are shown in Table 3. Based on considerations that the mechanisms that are responsible for the build-up of the central massive objects are similar for nuclei and massive BHs, previous studies have discussed their possible evolutionary connection (e.g., Ferrarese et al. 2006; Neumayer & Walcher 2012). For the purpose of comparison, we illustrate the black hole–galaxy mass relation from McConnell & Ma (2013) with its 1σ and 3σ uncertainty limits. This relation was obtained from fitting the compilation of 35 ETGs with dynamical measurements of the bulge stellar mass, with mass range of 10^9 to $10^{12}\,M_\odot$. Their sample is well populated for bulges more massive than $2 \times 10^{10}\,M_\odot$ (see their Figure 3). Assuming that we can extrapolate to lower bulge masses, we see in Figure 10 that the scaling relation for BHs and their ETG hosts is similar to the relation between nuclei and their host galaxy mass down to $10^9\,M_\odot$. For galaxies with lower masses, the nucleus-to-galaxy mass relation becomes flatter.

The mass ratio between nucleus and its host galaxy ($\eta_n = \mathcal{M}_{\rm nuc}/\mathcal{M}_{\rm gal}$) as a function of galaxy mass is shown at the bottom panel of Figure 10. We find a clear anticorrelation of η_n versus $\mathcal{M}_{\rm gal}$ over the entire galaxy mass range; that is, the lower the galaxy mass, the more significant becomes the nucleus. In the massive galaxy regime ($\mathcal{M}_{\rm gal} > 10^9\,M_\odot$), we note a large scatter in the relation, which is the main reason why previous studies assumed a constant equivalent luminosity ratio $\eta_{n,L} = \mathcal{L}_{\rm nuc}/\mathcal{L}_{\rm gal}$ for their samples, like for instance the ACS Virgo nucleated galaxies with $\langle\eta_{n,L}\rangle = 0.30\% \pm 0.04\%$ (Côté et al. 2006), $\langle\eta_{n,L}\rangle = 0.41\% \pm 0.04\%$ for the ACS Fornax nucleated galaxies (Turner et al. 2012), and $\langle\eta_{n,L}\rangle = 0.1\%$ for LTGs (Georgiev et al. 2016). However, in the faint dwarf galaxy regime ($\mathcal{M}_{\rm gal} \leqslant 10^9\,M_\odot$), a clear and strong trend appears, reaching to $\eta_n \simeq 10\%$ for a dwarf galaxy with a stellar mass of $10^7\,M_\odot$. The four low-mass ETGs studied by Nguyen et al. (2017, 2018) have η_n values up to 1.7%, which are in agreement with the general trend. The extension of the η_n versus $\mathcal{M}_{\rm gal}$ anticorrelation toward the faint dwarf galaxy population appears to be similar for ETGs and LTGs. This, in turn, suggests that nuclei at the smallest masses are subject to localized processes that work on parsec scales within the galaxy core regions independent of galaxy type.

5.3. Comparison with Theoretical Predictions

The two proposed formation scenarios for nuclei are globular cluster infall due to dynamical friction (Tremaine et al. 1975) and in situ star formation (van den Bergh 1986). The latter needs a mechanism to funnel gas into the galaxy center. Some studies suggest mechanisms to carry the gas inward to be galaxy mergers between two disk galaxies (Mihos & Hernquist 1994), supernova feedback outflows that become stalled because the intergalactic medium (IGM) pressure prevents the gas from escaping the dwarf galaxy (Babul92 & Rees 1992), and gas disks embedded in an old stellar spheroid (Bekki 2007). Observational studies for ETGs have argued that the predominant mechanism for nucleus formation in more massive galaxies is dissipative processes, sinking gas to the central galaxy regions with star formation occurring in situ, while for low-mass galaxies, nucleus formation occurs via GC infall due to short dynamical timescales (e.g., Lotz et al. 2004; Côté et al. 2006; Turner et al. 2012). In this context, we note that in the Virgo cluster, more than 50% of the bright early-type dwarfs were found to show underlying disk features, with the disk fraction decreasing to only a few percent for such dwarfs fainter than $M_B = -15.5$ mag (Lisker et al. 2006b), corresponding to $\log(\mathcal{M}_\star/M_\odot) \simeq 8.6$ (see Figure 7 in Eigenthaler et al. 2018). Moreover, about 15% of the Virgo early-type dwarfs brighter than $M_B = -15.5$ mag reveal blue centers, which were spectroscopically shown to correspond to recent star formation (Lisker et al. 2006a). In a more recent work, Spengler et al. (2017) compared their multiband photometry of nuclei with scaling relation predictions from Bekki (2007) and

Table 3
Scaling Relations

Fit	Parameters	Fornax	NGFS Dwarfs + ETGs	NGFS Dwarfs + LTGs
		$\mathcal{M}_{\rm nucleus}$ versus $\mathcal{M}_{\rm galaxy}$		
Linear regression	a	0.766 ± 0.048	0.723 ± 0.046	0.480 ± 0.033
$y = ax + b$	b	-0.096 ± 0.396	0.197 ± 0.392	1.850 ± 0.305
Polynomial fit degree = 3	a	0.068 ± 0.038	0.055 ± 0.038	0.031 ± 0.025
$y = ax^3 + bx^2 + cx + d$	b	-1.573 ± 0.946	-1.273 ± 0.976	-0.703 ± 0.654
	c	12.418 ± 7.881	10.245 ± 8.214	5.646 ± 5.685
	d	-28.085 ± 21.677	-22.923 ± 22.821	-10.212 ± 16.313
		$\eta_n = \mathcal{M}_{\rm nucleus}/\mathcal{M}_{\rm galaxy}$ versus $\mathcal{M}_{\rm galaxy}$		
Linear regression	a	-0.234 ± 0.048	-0.277 ± 0.046	-0.520 ± 0.033
$y = ax + b$	b	-0.096 ± 0.396	0.198 ± 0.392	1.850 ± 0.305
Polynomial fit degree = 3	a	0.069 ± 0.038	0.055 ± 0.038	0.031 ± 0.025
$y = ax^3 + bx^2 + cx + d$	b	-1.573 ± 0.946	-1.273 ± 0.976	-0.703 ± 0.654
	c	11.418 ± 7.881	9.245 ± 8.214	4.646 ± 5.685
	d	-28.087 ± 21.677	-22.924 ± 22.821	-10.212 ± 16.313

Note. For the nucleus versus galaxy mass relation ($\mathcal{M}_{\rm nucleus}$ versus $\mathcal{M}_{\rm galaxy}$), we set $y \equiv \log(\mathcal{M}_{\rm nucleus})$ and $x \equiv \log(\mathcal{M}_{\rm galaxy})$. For the mass ratio ($\eta_n$) relation as a function of galaxy mass (η_n versus $\mathcal{M}_{\rm galaxy}$), we define $y \equiv \log(\eta_n)$ and $x \equiv \log(\mathcal{M}_{\rm galaxy})$.

Antonini et al. (2015) and inferred that there is no single preferred formation scenario for nuclei, suggesting a mix of processes instead (see also Da Rocha et al. 2011). We proceed to compare the nucleus sample available for the Fornax cluster (NGFS and ACSFCS nuclei) with scaling relation predictions for different formation scenarios in an approach similar to that of Spengler et al. (2017). Figure 11 illustrates the comparison of empirical results with theoretical predictions.

5.3.1. Bekki Model Predictions

Pure dissipative models such as the one put forward by Bekki (2007), which takes into account feedback from SNe and supermassive BHs, depend mainly on the spheroid mass ($0.025 < \mathcal{M}_{\rm sph}/10^9 M_\odot < 5.0$), the initial gas mass fraction ($0.02 \leqslant f_{\rm gas} \leqslant 0.5$), the spheroid surface brightness (SB), and the chosen IMF (bottom- or top-heavy). Some of the more relevant nucleus properties in the numerical results of this model are that η_n can reach up to 5%, more massive spheroids have more metal-rich nuclei, and less massive spheroids can hold a young nucleus due to longer timescales of nucleus formation. Compared to the Fornax nucleated galaxy sample, the Bekki (2007) model (gray dashed curves in Figure 11) reproduces the η_n values for galaxies with masses of $\mathcal{M}_{\rm gal} \lesssim 10^8\,M_\odot$, but predicts too-massive nuclei in more massive galaxies relative to the observations. The predicted trend in the η_n–galaxy mass relation is too steep for massive nucleated galaxies, in contrast to the empirical results. Although the observed mass ratios reach up to 10%, they do so only at the lowest ($\sim 10^7\,M_\odot$) and highest sampled masses ($\gtrsim 10^{10}\,M_\odot$), while the model reaches those values at smaller masses. For masses of the order of $10^{9.5}\,M_\odot$, the mass ratio η_n for our sample is about one order of magnitude smaller than the predicted values. Clearly the theoretical ingredients of the Bekki (2007) model ought to be adjusted to better reproduce the observed hockey-stick trend of the η_n–$\mathcal{M}_{\rm gal}$ relation, where stronger suppression within the model framework of the

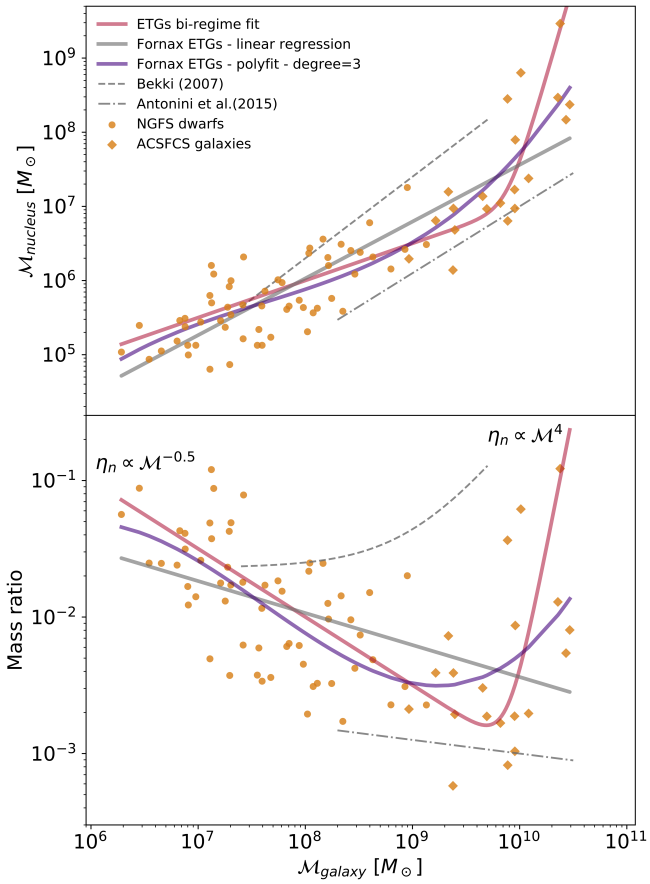

Figure 11. Scaling relations of the nucleus and galaxy masses. Top panel: nucleus vs. galaxy mass relation for all nucleated galaxies in the Fornax core region (NGFS dwarfs and ACSFCS sample). Bottom panel: nucleus-to-galaxy mass ratio ($\eta_n = \mathcal{M}_{\rm nuc}/\mathcal{M}_{\rm gal}$) as a function of galaxy mass. Solid lines show the weighted least-squares fits, the numerical values of which are shown in Table 3. Both panels show model predictions for nucleus formation. See the legend and text for more details.

nucleus mass accumulation process at intermediate masses (10^8–$10^{10}\,M_\odot$) seems necessary. In light of the relatively high fraction of disk components in intermediate-mass dwarfs (see Lisker et al. 2006b), this may be accomplished by either an enhanced disk/spheroid growth mode or suppression of the nuclear mass accumulation mechanism, such as via advective angular momentum transport, bar instabilities, or the presence of a central black hole (Curir et al. 2008; Curir et al. 2010; Foyle et al. 2010; Goz et al. 2015; James & Percival 2018).

5.3.2. Antonini Model Predictions

An hybrid approach to modeling the formation of galaxy nuclei was undertaken by Antonini et al. (2015), where two nucleus formation models are considered. The first model is the cluster-inspiral (CliN) model, which simulates star cluster mergers in the center of an isolated galaxy with a preexisting central BH. The second is a galaxy formation (GxeV) model, which tracks the evolution of baryonic structures in dark-matter merger trees. The GxeV model includes galaxy evolution, dissipative processes, mergers between galaxies, tidal interactions, and coexistence with supermassive BHs. This hybrid approach considers two possibilities for nucleus growth from high-redshift to the present day by migration of star clusters or in situ formation. The models CliN and GxeV have similar scaling relations, but GxeV has a larger dispersion in the nucleus masses than CliN does. In addition, CliN cannot form nuclei more massive than a few $10^7\,M_\odot$, but GxeV can. Antonini et al. (2015) tested the case without BH heating and found that both models still are able to form massive nuclei without any constraint on velocity dispersion or galaxy mass. One interesting prediction is that nuclei can be formed with one mechanism alone, the in situ star formation. However, a shallower slope is then obtained for the nucleus–galaxy mass relation relative to the scenario when both mechanisms are at work.

When comparing the predictions (CliN and GxeV are similar in this parameter space; dash-dotted lines in Figure 11) with Fornax nucleated galaxies, the predicted masses tend to be a factor of a few smaller than the observed ones over the mass range covered by the models ranging from $2 \times 10^8\,M_\odot$ to $3 \times 10^{10}\,M_\odot$. Antonini et al. (2015) noticed the offset and argue that the underweight of model nuclei is due to the interaction of the nucleus with the central massive BH, which makes the nucleus lose stars faster, in addition to galaxy mergers, where BH binaries form and efficiently eject surrounding stars. These effects have a greater impact in more massive galaxies than in low-mass dwarfs. The overall prediction by Antonini et al. (2015) is that both mechanisms are likely active during nucleus growth and that their relative contribution depends on the star-cluster formation efficiency. These models show that for galaxies less massive than $\sim 3 \times 10^{11}\,M_\odot$, in situ star formation contributes ~50% of the nucleus mass and becomes more important for more massive galaxies. This suggests that massive galaxies are more efficient in driving the gas flows to the galaxy core regions than are low-mass galaxies. This gas funneling allows for subsequent star formation to progress to more advanced stages, with implications for the resulting chemical makeup of the stellar populations, which would exhibit lower [α/Fe] element ratios.

In any case, the Antonini et al. (2015) models require modification in order to reproduce the sharp upturn of the observed η_n–$\mathcal{M}_{\rm gal}$ relation.

5.4. Correlation of the Nucleation Strength with the Spatial Distribution in Fornax

Figure 12 shows the spatial distribution of the galaxies in the central region of the Fornax cluster, where the nucleated galaxies from the NGFS and ACSFCS samples with mass ratio information are shown in orange symbols, while the rest of the dwarf galaxies are indicated by gray symbols. In this plot, the transparency of the symbols for the nucleated dwarfs is parameterized by the nucleus-to-galaxy mass ratio (η_n), as indicated in the legend in the top left corner. We find that dwarfs located closer to massive galaxies have mass ratios below 1%. However, we see that the dwarfs with the highest mass ratios in our sample are located on the edges of the field of view at the north and south directions.

In Section 4.3 we introduced two nucleated dwarf groups according to their stellar population parameters derived from SSP model predictions in the $u'i'Ks$ diagram. We defined group $\mathcal{B}$ of nuclei that appear younger and more metal-rich than the nuclei of group $\mathcal{A}$, which appear, on average, older and more metal-poor. The nuclei from group $\mathcal{B}$ are marked with purple ellipses in Figure 12, which reveal a strong asymmetry in their spatial distribution, where virtually all of the younger and metal-rich nuclei are located in an overdensity westward of the Fornax center. This suggests that dwarf galaxies in different regions of the Fornax cluster must have experienced different formation histories. We will test the significance of this overdensity once the dwarf sample from the entire NGFS footprint is available.

6. Conclusions

We have characterized 61 nuclear star clusters in the Fornax cluster region ($\leqslant R_{\rm vir}/4$). We used deep and homogeneous $u'g'i'JK_s$ photometry to obtain information on their luminosity and color distributions. In the following, we summarize our main results:

1. The nucleation fraction ($f_{\rm nuc}$) depends strongly on the galaxy luminosity, reaching $f_{\rm nuc} \geqslant 90\%$ for the bright NGFS dwarf galaxies ($M_{g'} \leqslant -16$ mag) and dropping to zero at absolute galaxy magnitudes fainter than $M_{g'} \simeq -10$ mag. The galaxy luminosity at which the nucleation stops corresponds to a stellar mass of $\log \mathcal{M}_* \simeq 6.4\,M_\odot$. As the NGFS data have a very faint point-source detection limits ($M_{g'} \approx -5.4$ mag), this is an astrophysical effect and clearly not related to observational constraints.
2. Color–magnitude diagrams using various filter combinations show that nuclei occupy the bluest parts in color space, but have a luminosity coverage comparable to the distribution of compact stellar systems in Fornax. The latter distribution is significantly broader, which is mainly due to the large spread in metal content. Nuclei in dwarf galaxies show a flat color–magnitude relation, which is opposite to the trend found for UCDs and the dwarf galaxy spheroids, which both show a positive color–luminosity relation.
3. We derive stellar masses for our nuclei with a mean uncertainty of ~19% and find that the nucleus stellar mass distribution covers the range $\log(\mathcal{M}_*/M_\odot) = 4.8$–$7.3$. We

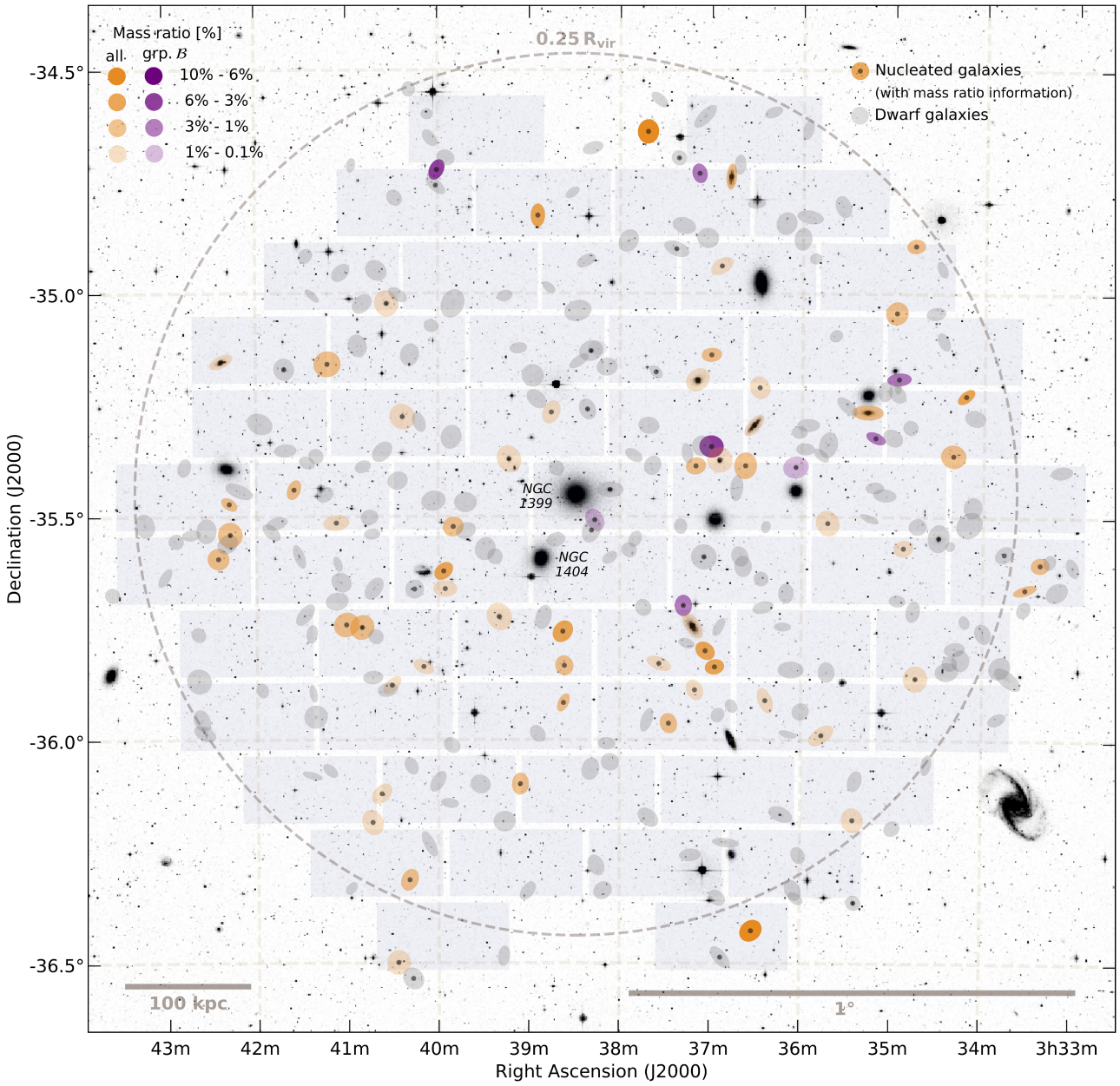

Figure 12. Illustration of the central region of the Fornax galaxy cluster showing the spatial distribution of nonnucleated (gray symbols) and nucleated dwarfs, which are shown as orange symbols (NGFS dEN and ACSFCS) if mass ratio information is available. Otherwise, they are shown in gray scale as well. The symbol transparency parameterizes the mass ratio as $\eta_n = \mathcal{M}_{\rm nuc}/\mathcal{M}_{\rm gal}$ ranging from 10% to 0.1% of the host galaxy mass, which is indicated in the top left corner. Group $\mathcal{B}$ nuclei (see Section 4.3), which are younger and more metal-rich than group $\mathcal{A}$, are shown in purple.

find that the nucleus mass distribution is bimodal, with peaks located at $\log(\mathcal{M}_*/M_\odot) \simeq 5.38$ and 6.25. The second peak is consistent with UCD masses. We derive stellar masses for our CSS comparison data set, which is limited at the low-mass end by the spectroscopic selection function.

4. The combination of the $u'i'K_s$ diagram with SSP model predictions reveals a bimodality in the stellar population parameters of nuclei, which is congruent with the two groups in the mass distribution function of NGFS nuclei. We define two groups, with group $\mathcal{A}$ comprising nuclei with colors $(u'-i')_0 < 2.0$ mag and $(i'-K_s)_0 < -0.2$ mag, which according to SSP models are consistent with metal-poor stellar populations ($Z < 0.02\,Z_\odot$) and ages older than 2 Gyr. The nuclei in group $\mathcal{A}$ have stellar masses $>10^6\,M_\odot$. Group $\mathcal{B}$ contains less massive objects and covers a more extended region in the $u'i'K_s$ color space with redder average colors, an indication of a larger range in metallicity $0.2 < Z/Z_\odot < 1$ and ages younger than 2 Gyr. With the exception of one object, the masses of the group $\mathcal{B}$ nuclei are all $<10^6\,M_\odot$.
5. Dividing the CSS sample confirmed by radial velocity into GCs and UCDs using a stellar mass cut at $\log(\mathcal{M}_*/M_\odot) = 6.3$ shows that the low-mass modes of our sample nuclei (group $\mathcal{B}$) cannot be progenitors of Fornax UCDs. On the other hand, the high-mass-mode nuclei located in bright galaxies could be potential progenitors of metal-poor UCDs. Notwithstanding this, our NGFS nuclei could all

be considered as potential future GCs, once their host galaxy spheroids are stripped by the dynamical evolution of the system inside the Fornax cluster environment.

6. Color differences between the nucleus and its parent galaxy spheroid correlate more with the spheroid light than with the nucleus luminosity. Therefore, the mechanism that produces these color offsets is more likely to be acting on galaxy scales. Colors with a wide SED coverage, such as $\Delta(u'-i')_0$ and $\Delta(u'-g')_0$, are more sensitive to changes in stellar populations and show a steeper relation with spheroid luminosity than $\Delta(g'-i')_0$. Bright nuclei tend to be bluer than their host galaxy. Nonetheless, as we sample fainter galaxy luminosities, we find a transition point where the color offset becomes more stochastic, and we find both bluer and redder nuclei than their host. This transition occurs at $M_{g',\mathrm{nuc}} \simeq -7.5$ or $M_{g',\mathrm{sph}} \simeq -12.5$ for $\Delta(g'-i')_0$ and $M_{g',\mathrm{nuc}} \simeq -9.5$ or $M_{g',\mathrm{sph}} \simeq -14.0$ for $\Delta(u'-i')_0$ and $\Delta(u'-g')_0$.
7. Scaling relations such as the nucleus-to-galaxy mass relation ($\mathcal{M}_{\mathrm{nuc}}$ versus $\mathcal{M}_{\mathrm{gal}}$) show a clear mass correlation between nuclei and their host galaxy over the entire mass range of our NGFS sample. This relation shows a break in the slope at $\log(\mathcal{M}_*/M_\odot) \simeq 9.7$, where we find a shallower slope for dwarf galaxies relative to their more massive counterparts. Comparing with the BH–galaxy mass relation, we find that it has a relation similar to the nuclei and their host galaxy mass down to $10^9\,M_\odot$. For galaxies with lower masses, their nucleus–galaxy mass scaling relation becomes flatter than the BH–galaxy mass relation. For the nuclei-to-galaxy mass ratio versus galaxy mass relation ($\eta_n = \mathcal{M}_{\mathrm{nucleus}}/\mathcal{M}_{\mathrm{galaxy}}$ versus $\mathcal{M}_{\mathrm{galaxy}}$), an interesting anticorrelation is found. The lower the galaxy mass, the more prominent the nucleus becomes, with a scaling $\eta_n \propto \mathcal{M}_{\mathrm{gal}}^{-0.5}$. For masses higher than the break at $\log(\mathcal{M}_*/M_\odot) \simeq 9.7$, we find a positive correlation of the form $\eta_n \propto \mathcal{M}_{\mathrm{gal}}^{4}$. These relatively strong trends for low-mass and high-mass galaxies reach values up to $\eta_n \simeq 10\%$ for dwarf galaxies with a stellar mass of $10^7\,M_\odot$ and massive ellipticals at $10^{11}\,M_\odot$. The low-mass anticorrelation seems to be similar for ETGs and LTGs, suggesting that it is independent of galaxy type.
8. The spatial distribution of the Fornax nucleated dwarfs shows that they are preferentially distributed along the east–west direction. Knowing the location of the nucleated dwarfs with the highest η_n values, we observe that they lie at the edges of the central NGFS footprint to the north and south. We also find that the nuclei that are members of group $\mathcal{B}$ that are relatively metal-rich and have ages younger than 2 Gyr lie predominantly westward of NGC 1399, suggesting a more extended star formation history of nuclei in that direction.

Our NGFS study has extended the galaxy nucleus research toward the faint galaxy luminosity regime down to $\log(\mathcal{M}_*/M_\odot) \simeq 6$, finding nucleus–galaxy scaling relations that are quite different from the results obtained from bright galaxies. Theoretical models still fail to explain the observed scaling relations for the low-mass regime and do not account for the apparent transition between low-mass and high-mass galaxies. However, we find that the models by Bekki (2007) and Antonini et al. (2015) appear to frame our observations, which may indicate that a combination of their prescriptions may best represent reality. Overall, our NGFS nucleus sample gives crucial insights into the formation mechanism at work, showing that nuclei are likely formed via two different mechanisms: formation via dynamical friction acting on GCs sinking to the center and star formation processes in the central regions. The full NGFS footprint will provide a larger sample and help us to better understand the fascinating properties and the formation mechanisms of the nucleus population in dwarf galaxies.

This project is supported by FONDECYT Regular Project No. 1161817 and the BASAL Center for Astrophysics and Associated Technologies (PFB-06). Y.O.-B. acknowledges financial support through CONICYT-Chile (grant CONICYT-PCHA/Doctorado Nacional No. 2014-21140651) and the DAAD through the PUC-HD Graduate Exchange Fellowship. T.H.P. and A.L. gratefully acknowledge ECOS-Sud/CONICYT project C15U02. P.E. acknowledges support from the Chinese Academy of Sciences (CAS) through CAS-CONICYT Postdoctoral Fellowship CAS150023 administered by the CAS South America Center for Astronomy (CAS-SACA) in Santiago, Chile. M.A.T. is supported by the Gemini Observatory, which is operated by the Association of Universities for Research in Astronomy, Inc., on behalf of the international Gemini partnership of Argentina, Brazil, Canada, Chile, and the United States of America.

This project used data obtained with the Dark Energy Camera (DECam), which was constructed by the Dark Energy Survey (DES) collaboration. This research has made use of the NASA Astrophysics Data System Bibliographic Services, the NASA Extragalactic Database, the SIMBAD database, operated at CDS, Strasbourg, France (Wenger et al. 2000). This research has made use of "Aladin Sky Atlas" (Bonnarel et al. 2000; Boch & Fernique 2014), developed at CDS, Strasbourg Observatory, France. Software used in the analysis includes the PYTHON/NUMPY v.1.11.2 and PYTHON/SCIPY v0.17.1 (Jones et al. 2001; VanderPlas et al. 2012, http://www.scipy.org/), PYTHON/ASTROPY (v1.2.1; Astropy Collaboration et al. 2013, http://www.astropy.org/), PYTHON/MATPLOTLIB (v2.0.0; Hunter 2007, http://matplotlib.org/), and PYTHON/SCIKIT-LEARN (v0.17.1; Pedregosa et al. 2012, http://scikit-learn.org/stable/) packages. This research made use of ds9, a tool for data visualization supported by the *Chandra* X-ray Science Center (CXC) and the High Energy Astrophysics Science Archive Center (HEASARC) with support from the *JWST* Mission office at the Space Telescope Science Institute for 3D visualization.

Facility: CTIO (4 m Blanco/DECam).

ORCID iDs

Yasna Ordenes-Briceño https://orcid.org/0000-0001-7966-7606
Thomas H. Puzia https://orcid.org/0000-0003-0350-7061
Paul Eigenthaler https://orcid.org/0000-0001-8654-0101
Matthew A. Taylor https://orcid.org/0000-0003-3009-4928
Roberto P. Muñoz https://orcid.org/0000-0003-1743-0456
Hongxin Zhang https://orcid.org/0000-0003-1632-2541
Karla Alamo-Martínez https://orcid.org/0000-0002-5897-7813
Karen X. Ribbeck https://orcid.org/0000-0002-3004-4317
Eva K. Grebel https://orcid.org/0000-0002-1891-3794
Simón Ángel https://orcid.org/0000-0002-5322-9189

Patrick Côté https://orcid.org/0000-0003-1184-8114
Laura Ferrarese https://orcid.org/0000-0002-8224-1128
Michael Hilker https://orcid.org/0000-0002-2363-5522
Ariane Lançon https://orcid.org/0000-0002-7214-8296
Steffen Mieske https://orcid.org/0000-0003-4197-4621
Bryan W. Miller https://orcid.org/0000-0002-5665-376X
Yu Rong https://orcid.org/0000-0002-2204-6558
Ruben Sánchez-Janssen https://orcid.org/0000-0003-4945-0056

References

Abazajian, K. N., Adelman-McCarthy, J. K., Agüeros, M. A., et al. 2009, ApJS, 182, 543
Antonini, F. 2013, ApJ, 763, 62
Antonini, F., Barausse, E., & Silk, J. 2015, ApJ, 812, 72
Arca-Sedda, M., & Capuzzo-Dolcetta, R. 2014, MNRAS, 444, 3738
Astropy Collaboration, Robitaille, T. P., Tollerud, E. J., et al. 2013, A&A, 558, A33
Babul92, A., & Rees, M. J. 1992, MNRAS, 255, 346
Bassino, L. P., Muzzio, J. C., & Rabolli, M. 1994, ApJ, 431, 634
Bekki, K. 2007, PASA, 24, 77
Bekki, K., Couch, W. J., & Drinkwater, M. J. 2001, ApJL, 552, L105
Bekki, K., Couch, W. J., Drinkwater, M. J., & Shioya, Y. 2003, MNRAS, 344, 399
Bell, E. F., McIntosh, D. H., Katz, N., & Weinberg, M. D. 2003, ApJS, 149, 289
Bertin, E. 2006, in ASP Conf. Ser. 351, Astronomical Data Analysis Software and Systems XV, ed. C. Gabriel et al. (San Francisco, CA: ASP), 112
Bertin, E., & Arnouts, S. 1996, A&AS, 117, 393
Bertin, E., Mellier, Y., Radovich, M., et al. 2002, in ASP Conf. Ser. 281, Astronomical Data Analysis Software and Systems XI, ed. D. A. Bohlender, D. Durand, & T. H. Handley (San Francisco, CA: ASP), 228
Blakeslee, J. P., Jordán, A., Mei, S., et al. 2009, ApJ, 694, 556
Blanton, M. R., & Roweis, S. 2007, AJ, 133, 734
Boch, T., & Fernique, P. 2014, in ASP Conf. Ser. 485, Astronomical Data Analysis Software and Systems XXIII, ed. N. Manset & P. Forshay (San Francisco, CA: ASP), 277
Böker, T., Sarzi, M., McLaughlin, D. E., et al. 2004, AJ, 127, 105
Bonnarel, F., Fernique, P., Bienaymé, O., et al. 2000, A&AS, 143, 33
Bruzual, G., & Charlot, S. 2003, MNRAS, 344, 1000
Cerviño, M., & Luridiana, V. 2004, A&A, 413, 145
Cerviño, M., Valls-Gabaud, D., Luridiana, V., & Mas-Hesse, J. M. 2002, A&A, 381, 51
Cleveland, W. 1981, Am. Stat., 35, 54
Côté, P., Piatek, S., Ferrarese, L., et al. 2006, ApJS, 165, 57
Curir, A., de Romeri, V., & Murante, G. 2010, Ap&SS, 327, 259
Curir, A., Mazzei, P., & Murante, G. 2008, A&A, 481, 651
Da Rocha, C., Mieske, S., Georgiev, I. Y., et al. 2011, A&A, 525, A86
de Boer, T. J. L., Belokurov, V., & Koposov, S. 2015, MNRAS, 451, 3489
den Brok, M., Peletier, R. F., Seth, A., et al. 2014, MNRAS, 445, 2385
Dotter, A., Sarajedini, A., & Anderson, J. 2011, ApJ, 738, 74
Drinkwater, M. J., Gregg, M. D., & Colless, M. 2001, ApJL, 548, L139
Eigenthaler, P., Puzia, T. H., Taylor, M. A., et al. 2018, ApJ, 855, 142
Evstigneeva, E. A., Gregg, M. D., Drinkwater, M. J., & Hilker, M. 2007, AJ, 133, 1722
Ferrarese, L., Côté, P., Cuillandre, J.-C., et al. 2012, ApJS, 200, 4
Ferrarese, L., Côté, P., Dalla Bontà, E., et al. 2006, ApJL, 644, L21
Fitzpatrick, E. L. 1999, PASP, 111, 63
Flaugher, B., Diehl, H. T., Honscheid, K., et al. 2015, AJ, 150, 150
Forbes, D. A., & Bridges, T. 2010, MNRAS, 404, 1203
Fouesneau, M., & Lançon, A. 2010, A&A, 521, A22
Foyle, K., Rix, H.-W., & Zibetti, S. 2010, MNRAS, 407, 163
Francis, K. J., Drinkwater, M. J., Chilingarian, I. V., Bolt, A. M., & Firth, P. 2012, MNRAS, 425, 325
Georgiev, I. Y., & Böker, T. 2014, MNRAS, 441, 3570
Georgiev, I. Y., Böker, T., Leigh, N., Lützgendorf, N., & Neumayer, N. 2016, MNRAS, 457, 2122
Georgiev, I. Y., Hilker, M., Puzia, T. H., Goudfrooij, P., & Baumgardt, H. 2009, MNRAS, 396, 1075
Goerdt, T., Moore, B., Kazantzidis, S., et al. 2008, MNRAS, 385, 2136
Goz, D., Monaco, P., Murante, G., & Curir, A. 2015, MNRAS, 447, 1774
Hansson, K. S. A., Lisker, T., & Grebel, E. K. 2012, MNRAS, 427, 2376
Hunter, J. D. 2007, CSE, 9, 90
Ivezić, Ž., Connolly, A., Vanderplas, J., & Gray, A. 2014, Statistics, Data Mining and Machine Learning in Astronomy (Princeton, NJ: Princeton Univ. Press)
James, P. A., & Percival, S. M. 2018, MNRAS, 474, 3101
Jones, E., Oliphant, T., Peterson, P., et al. 2001, SciPy: Open Source Scientific Tools for Python, http://www.scipy.org/
Kawakatu, N., & Umemura, M. 2002, MNRAS, 329, 572
Kewley, L. J., & Ellison, S. L. 2008, ApJ, 681, 1183
Kim, H.-S., Yoon, S.-J., Sohn, S. T., et al. 2013, ApJ, 763, 40
Kissler-Patig, M., Brodie, J. P., Schroder, L. L., et al. 1998, AJ, 115, 105
Kodama, T., & Arimoto, N. 1997, A&A, 320, 41
Kormendy, J., & Ho, L. C. 2013, ARA&A, 51, 511
Kroupa, P. 2001, MNRAS, 322, 231
Leaman, R., VandenBerg, D. A., & Mendel, J. T. 2013, MNRAS, 436, 122
Lisker, T., Glatt, K., Westera, P., & Grebel, E. K. 2006a, AJ, 132, 2432
Lisker, T., Grebel, E. K., & Binggeli, B. 2006b, AJ, 132, 497
Lotz, J. M., Miller, B. W., & Ferguson, H. C. 2004, ApJ, 613, 262
Lotz, J. M., Telford, R., Ferguson, H. C., et al. 2001, ApJ, 552, 572
Ma, J., van den Bergh, S., Wu, H., et al. 2006, ApJL, 636, L93
Marín-Franch, A., Aparicio, A., Piotto, G., et al. 2009, ApJ, 694, 1498
Matteucci, F., & Greggio, L. 1986, A&A, 154, 279
Matteucci, F., & Recchi, S. 2001, ApJ, 558, 351
McConnell, N. J., & Ma, C.-P. 2013, ApJ, 764, 184
Mieske, S., Frank, M. J., Baumgardt, H., et al. 2013, A&A, 558, A14
Mihos, J. C., Harding, P., Feldmeier, J., & Morrison, H. 2005, ApJL, 631, L41
Mihos, J. C., Harding, P., Feldmeier, J. J., et al. 2017, ApJ, 834, 16
Mihos, J. C., & Hernquist, L. 1994, ApJL, 437, L47
Misgeld, I., & Hilker, M. 2011, MNRAS, 414, 3699
Muñoz, R. P., Eigenthaler, P., Puzia, T. H., et al. 2015, ApJL, 813, L15
Muñoz, R. P., Puzia, T. H., Lançon, A., et al. 2014, ApJS, 210, 4
Neumayer, N., & Walcher, C. J. 2012, AdAst, 2012, 709038
Nguyen, D. D., Seth, A. C., den Brok, M., et al. 2017, ApJ, 836, 237
Nguyen, D. D., Seth, A. C., Neumayer, N., et al. 2018, ApJ, 858, 118
Paudel, S., Lisker, T., & Janz, J. 2010, ApJL, 724, L64
Paudel, S., Lisker, T., & Kuntschner, H. 2011, MNRAS, 413, 1764
Pedregosa, F., Varoquaux, G., Gramfort, A., et al. 2012, JMLR, 12, 2825
Peng, C. Y., Ho, L. C., Impey, C. D., & Rix, H.-W. 2002, AJ, 124, 266
Pfeffer, J., & Baumgardt, H. 2013, MNRAS, 433, 1997
Powalka, M., Lançon, A., Puzia, T. H., et al. 2016a, ApJS, 227, 12
Powalka, M., Lançon, A., Puzia, T. H., et al. 2017, ApJ, 844, 104
Powalka, M., Puzia, T. H., Lançon, A., et al. 2016b, ApJL, 829, L5
Puzia, T. H., Kissler-Patig, M., Thomas, D., et al. 2005, A&A, 439, 997
Puzia, T. H., Paolillo, M., Goudfrooij, P., et al. 2014, ApJ, 786, 78
Rejkuba, M. 2012, Ap&SS, 341, 195
Roediger, J. C., Ferrarese, L., Côté, P., et al. 2017, ApJ, 836, 120
Rossa, J., van der Marel, R. P., Böker, T., et al. 2006, AJ, 132, 1074
Sánchez-Blázquez, P., Peletier, R. F., Jiménez-Vicente, J., et al. 2006, MNRAS, 371, 703
Schlafly, E. F., & Finkbeiner, D. P. 2011, ApJ, 737, 103
Schlegel, D. J., Finkbeiner, D. P., & Davis, M. 1998, ApJ, 500, 525
Schödel, R., Feldmeier, A., Kunneriath, D., et al. 2014, A&A, 566, A47
Skrutskie, M. F., Cutri, R. M., Stiening, R., et al. 2006, AJ, 131, 1163
Smith, R., Sánchez-Janssen, R., Beasley, M. A., et al. 2015, MNRAS, 454, 2502
Smith, R., Sánchez-Janssen, R., Fellhauer, M., et al. 2013, MNRAS, 429, 1066
Spengler, C., Côté, P., Roediger, J., et al. 2017, ApJ, 849, 55
Sutherland, W., Emerson, J., Dalton, G., et al. 2015, A&A, 575, A25
Taylor, M. A., Puzia, T. H., Harris, G. L., et al. 2010, ApJ, 712, 1191
Thomas, D., Maraston, C., Bender, R., & Mendes de Oliveira, C. 2005, ApJ, 621, 673
Torrey, P., Vogelsberger, M., Marinacci, F., et al. 2017, arXiv:1711.05261
Tremaine, S. D., Ostriker, J. P., & Spitzer, L., Jr. 1975, ApJ, 196, 407
Tremonti, C. A., Heckman, T. M., Kauffmann, G., et al. 2004, ApJ, 613, 898
Tsujimoto, T., Nomoto, K., Yoshii, Y., et al. 1995, MNRAS, 277, 945
Turner, M. L., Côté, P., Ferrarese, L., et al. 2012, ApJS, 203, 5
Valdes, F., Gruendl, R. & DES Project 2014, in ASP Conf. Ser. 85, Astronomical Data Analysis Software and Systems XXIII, ed. N. Manset & P. Forshay (San Francisco, CA: ASP), 379
van den Bergh, S. 1986, AJ, 91, 271
VandenBerg, D. A., Brogaard, K., Leaman, R., & Casagrande, L. 2013, ApJ, 775, 134
VanderPlas, J., Connolly, A. J., Ivezic, Z., & Gray, A. 2012, in Proc. of Conf. on Intelligent Data Understanding (CIDU), 47
Walcher, C. J., Böker, T., Charlot, S., et al. 2006, ApJ, 649, 692
Wenger, M., Ochsenbein, F., Egret, D., et al. 2000, A&AS, 143, 9

Willman, B., & Strader, J. 2012, AJ, 144, 76
Wittmann, C., Lisker, T., Pasquali, A., Hilker, M., & Grebel, E. K. 2016, MNRAS, 459, 4450
Zhang, H.-X., Puzia, T. H., & Weisz, D. R. 2017, ApJS, 233, 13
Zinnecker, H., Keable, C. J., Dunlop, J. S., Cannon, R. D., & Griffiths, W. K. 1988, in IAU Symp. 126, The Harlow-Shapley Symposium on Globular Cluster Systems in Galaxies, ed. J. E. Grindlay & A. G. D. Philip (Dordrecht: Kluwer Academic), 603